Shocked Clouds in the Vela Supernova Remnant

Joy S. Nichols

Harvard-Smithsonian Center for Astrophysics, 60 Garden Street, MS 34, Cambridge, MA 02138

jnichols@cfa.harvard.edu

and

Jonathan D. Slavin

Harvard-Smithsonian Center for Astrophysics, 60 Garden Street, MS 34, Cambridge, MA 02138

jslavin@cfa.harvard.edu

ABSTRACT

Unusually strong high-excitation C I has been detected in eleven lines of sight through the Vela supernova remnant by means of UV absorption-line studies of IUE data. Most of these lines of sight lie near the western edge of the X-ray bright region of the supernova remnant in a spatially distinct band approximately 1° by 4°oriented approximately north/south. The high-excitation C I (denoted C I*) is interpreted as evidence of a complex of shocked dense clouds inside the supernova remnant, due to the high pressures indicated in this region. To further analyze the properties of this region of C I*, we present new HIRES-processed IRAS data of the entire Vela SNR. A temperature map calculated from the HIRES IRAS data, based on a two-component dust model, reveals the signature of hot dust at several locations in the SNR. The hot dust is anti-correlated spatially with X-ray emission as revealed by ROSAT, as would be expected for a dusty medium interacting with a shock wave. The regions of hot dust are strongly correlated with optical filaments, supporting a scenario of dense clouds interior to the SNR that have been shocked and are now cooling behind the supernova blast wave. With few exceptions, the lines of sight to the strong C I* pass through regions of hot dust and optical filaments. Possible mechanisms for the production of the anomalously large columns of C I and C I* are discussed. Dense clouds on the back western hemisphere of the remnant may explain the relatively low X-ray emission in the western portion of the Vela supernova remnant due to the slower

forward shock velocity in regions where the shock has encountered the dense clouds. An alternate explanation for the presence of neutral, excited state, and ionized species along the same line of sight may be a magnetic precusor that heats and compresses the gas ahead of the shock.

1. Introduction

The interaction of supernova remnants (SNRs) with the surrounding ISM is fundamental to the understanding of the physical and chemical evolution of the galactic ISM, and to the dynamics and distribution of the hot gas in the Galaxy. A SNR in a cloudy medium will have a different evolution than one in a uniform ambient medium due changes in the shock front as it encounters the denser cloud material, causing a slower forward shock with accompanying higher densities and pressures (McKee & Cowie 1975; White & Long 1991). Considerable attention as been focused on the derivation of models of supernovae erupting in a non-uniform medium, for example Poludnenko et al. (2002),Klein et al. (1994). Dust in the evolving SNR will also have significant effects as the dust is first heated and then destroyed by the shock wave (Vancura et al. 1994).

The Vela SNR is one of the most frequently studied SNRs due to its proximity (250 pc, Cha & Sembach 2000), and large angular size of more than 7.3°. Raymond et al. (1997) find a shock velocity of 165 km s^{-1} for a face-on shock near the center of the remnant. For another region west of the center of the remnant, Raymond et al. (1991) determined a shock velocity of 150 km s^{-1}, with some evidence for thermally unstable cooling of the shocked gas. Recent UV absorption-line studies of O VI and C IV (Slavin et al. 2004) are consistent with the interpretation of a 150 km s^{-1} shock near the region studied by Raymond et al. (1991).

The Vela SNR has been the subject of a number of absorption-line studies using the bright background stars, with remarkable results. The number of components and the velocity range of high-velocity features in the optical and UV absorption lines for lines of sight through the Vela SNR are exceeded only in the Carina Nebula region (Walborn & Hesser 1982; Walborn et al. 1984).

Several studies of the interstellar absorption-line data in optical wavelengths have shown the presence of multiple high-velocity features to the Ca II and Na I lines (Wallerstein & Silk 1971; Wallerstein et al. 1980; Jenkins et al. 1984; Hobbs et al. 1991; Danks & Sembach 1995; Cha & Sembach 2000). Time variability of the absorption lines with time scales of a few years (Hobbs et al. 1991; Danks & Sembach 1995; Cha & Sembach 2000) has been seen

toward several targets in the line of sight to the Vela SNR. UV high-velocity absorption-line data for low- and high-ionization species have shown a velocity range of -90 to +180 km s^{-1} through many lines of sight toward this SNR (Jenkins et al. 1984). Surprisingly, they found no geometric expansion effects in their velocity data.

Unusually strong high-excitation lines of C I (denoted /CIstar) were first recognized in the IUE spectra of HD 72350 (Jenkins et al. 1981). These authors concluded the C I* originates in a dense cloud compressed by the supernova blast wave. Later observations of another star with strong C I* toward the Vela SNR, HD 72089, with GHRS (Jenkins & Wallerstein 1995) and with STIS (Jenkins et al. 1998) revealed 6 separate velocity components associated with each of the multiplet members of C I, both ground and excited state, with a velocity range of +1 - +121.5 km s^{-1}. The large column densities of the C I* high-velocity components at +85 and +121.5 km s^{-1} indicate high pressure and density. The presence of high-excitation and high-velocity C I led Jenkins & Wallerstein (1995) to conclude that there is a dense cloud in this line of sight which has been shocked by the supernova blast wave. Two additional stars in the Vela SNR line of sight have been observed with GHRS on HST in the C I lines. HD 72127A was found to have two high-velocity components in the at +7 and +52 km s^{-1}, while its visual binary companion, HD 72127B exhibited only single components.

Dense clouds that have been shocked and are cooling are expected to be the site of emission from several ionization species as the gas recombines behind the shock wave. The high pressure and density near the surface of shocked clouds can produce high column densities of [O III] (McKee & Cowie (1975); Fesen et al. (1982)) as well as C I* (Jenkins & Wallerstein 1995). Such dense clouds will slow the forward shock wave and produce a reverse shock, altering the temperature, density, and pressure of the local environment in the SNR.

We report the presence of anomalously strong C I* lines in the four C I multiplets found in high-resolution IUE observations of 11 stars in the line of sight to the Vela SNR, based on analysis of 53 IUE spectra of stars behind the Vela SNR. We also present new HIRES-processed IRAS data of the entire Vela SNR that are used to search for the signature of hot dust associated with the remnant. Section 2 describes the observations and analysis techniques for the IUE and IRAS data. Section 3 discusses the spatial distribution of the C I* in relation to the IR, X-ray, and optical emission. A temperature map of the HIRES IRAS data is presented. Possible sources of the enhanced C I and C I* are considered. Conclusions are presented in Section 4.

2. Observations

2.1. C I* Data from IUE

We have examined the high-resolution IUE spectra of 53 stars in the line of sight to the Vela SNR. These stars are listed in Table 1, along with their coordinates, spectral types, Hipparcos distances (if available), spectroscopic distances, IUE image sequence numbers of the data analyzed, and observation date. Spectroscopic distances were determined using (B-V) measurements as preferred in the SIMBAD database, and the M_v calibration of Lesh (1982) and the $(B-V)_0$ calibration of Fitzgerald (1970). A value of 3.1 was adopted for R. We have selected all high-resolution spectra from the Short Wavelength Prime (SWP) IUE camera of hot stars in the IUE archive in the range $258° \leq l_{II} \leq 269°$ and $-8° \leq b_{II} \leq +2°$ for study of the Vela SNR. The positions of these stars are shown in Figure 1, with the ROSAT X-ray contours superimposed for reference. While the sampling of the region is generally quite good, there are a few unsampled pockets evident in the figure, particularly at approximately 1° west and 1° east of the Vela pulsar. The lack of data in these regions must be considered in the conclusions to this work.
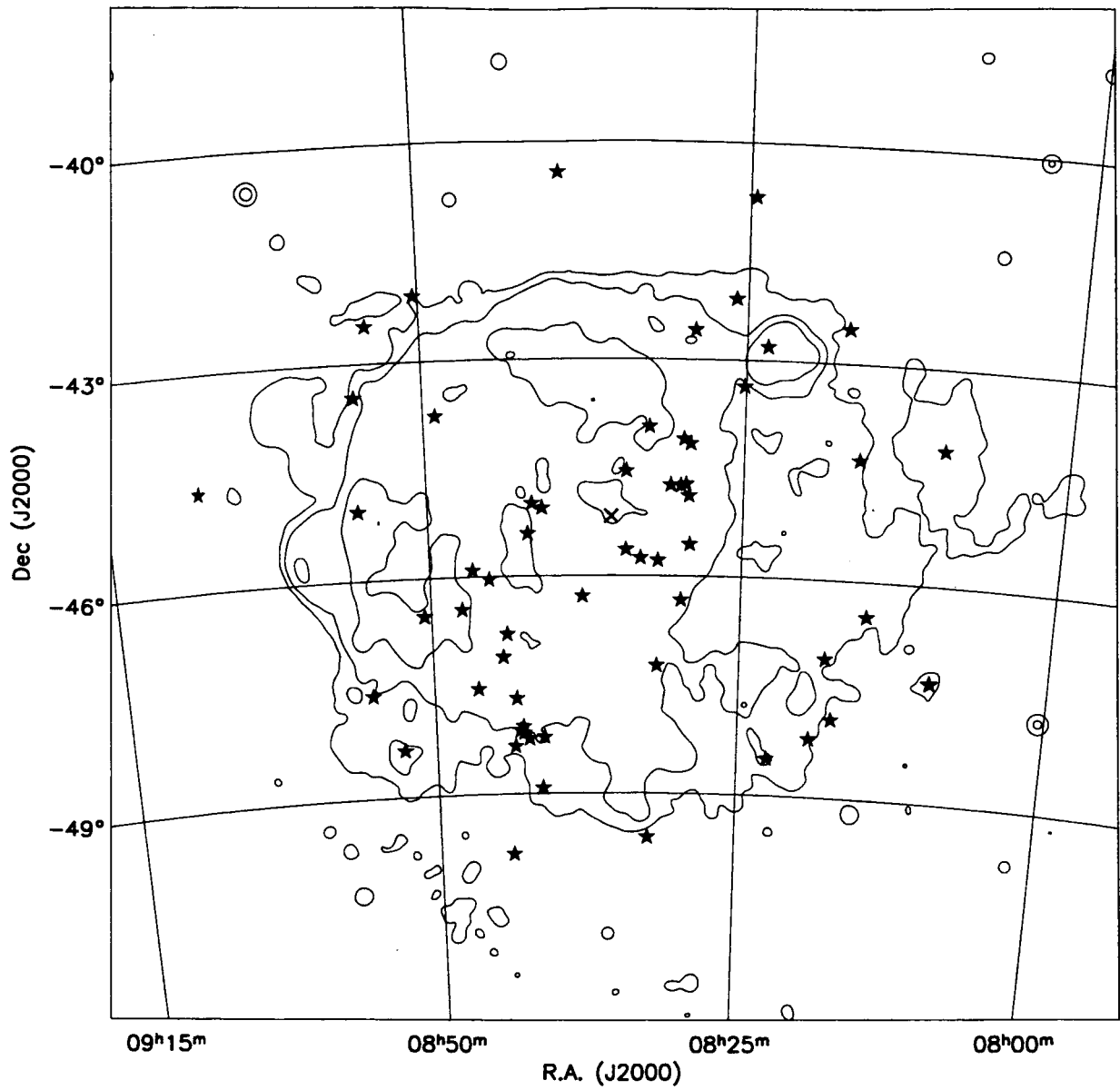
Fig. 1.— X-ray contours derived from the ROSAT all-sky survey image of the Vela SNR with all of the stars observed with IUE in this region overplotted. The position of the Vela pulsar is indicated with an "x" symbol.

The resolution of IUE (R = 10,000) is not sufficient to measure reliably the equivalent widths of the individual members of each C I multiplet in many cases. More importantly, based on Jenkins & Wallerstein (1995), high-velocity features may contaminate neighboring lines in the multiplets, rendering equivalent width measurement misleading. We chose to measure only the velocity displacements from rest wavelength of C I features for the ground and strongest high-excitation lines (if detectable) in each multiplet. There are four C I multiplets available in the IUE data, all of which fall in the wavelength regime of the SWP camera. Table 2 lists the four multiplets analyzed and the wavelengths of each component of the multiplets. The velocity displacement from the ground state component for each of the high-excitation lines is also listed for reference. These wavelength displacements served as a guide to determine if the features we detected were indeed C I*.

The four C I multiplets examined in our analysis are each the ground state transition in multiplets of up to five transitions. Members of some of the multiplets are so closely spaced that they cannot be easily resolved with IUE data. In addition, any high-velocity features would be too blended to separate. However, each of the four multiplets has a different set of component wavelength displacements, as seen in Table 2, so that strong features detected can be compared to these velocity displacements. Occasionally, however, the wavelength region of a multiplet was too confused to measure any component.

Eleven of the 53 stars studied showed evidence of strong C I* in their spectra. Our criterion for identifying unusually strong C I* was a minimum flux approximately equal to 30% or greater of the minimum flux of the ground state C I line of the multiplet. The potential presence of high-velocity features prevented us from using equivalent width or column-density measurements as a criterion. Also, the possibility of time variability deterred us from co-adding all available spectra of an object for this analysis. Only one spectrum of each object was used in the analysis, even if more were available. Figures 2-5 are montages of the 11 spectra for the 1657Å and 1329Å C I multiplets in the IUE wavelength region. The location of each member of the multiplet has been indicated, along with its J value. We used the IUESIPS version of the IUE data processing for this analysis. For purposes of detecting weak absorption features, the oversampling of IUESIPS is preferable because some narrow features that are actually real can be smoothed to the point of nondetection with NEWSIPS.
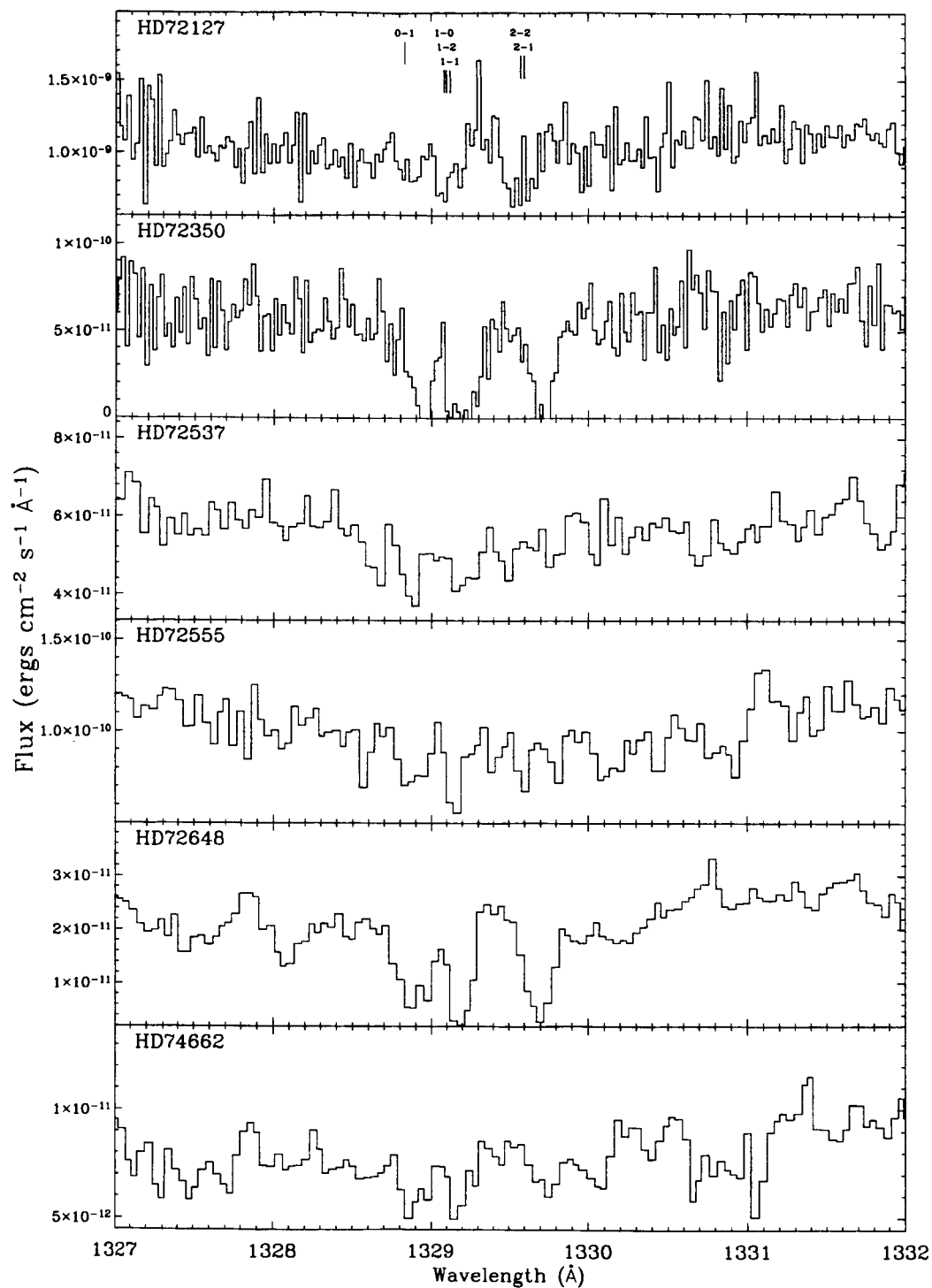
Fig. 2.— Montage of the spectral region near the 1392 Å C I multiplet in IUE high-resolution data (for the first five stars in our data set). The rest wavelengths of the transitions are indicated and labeled by the J values of the states.
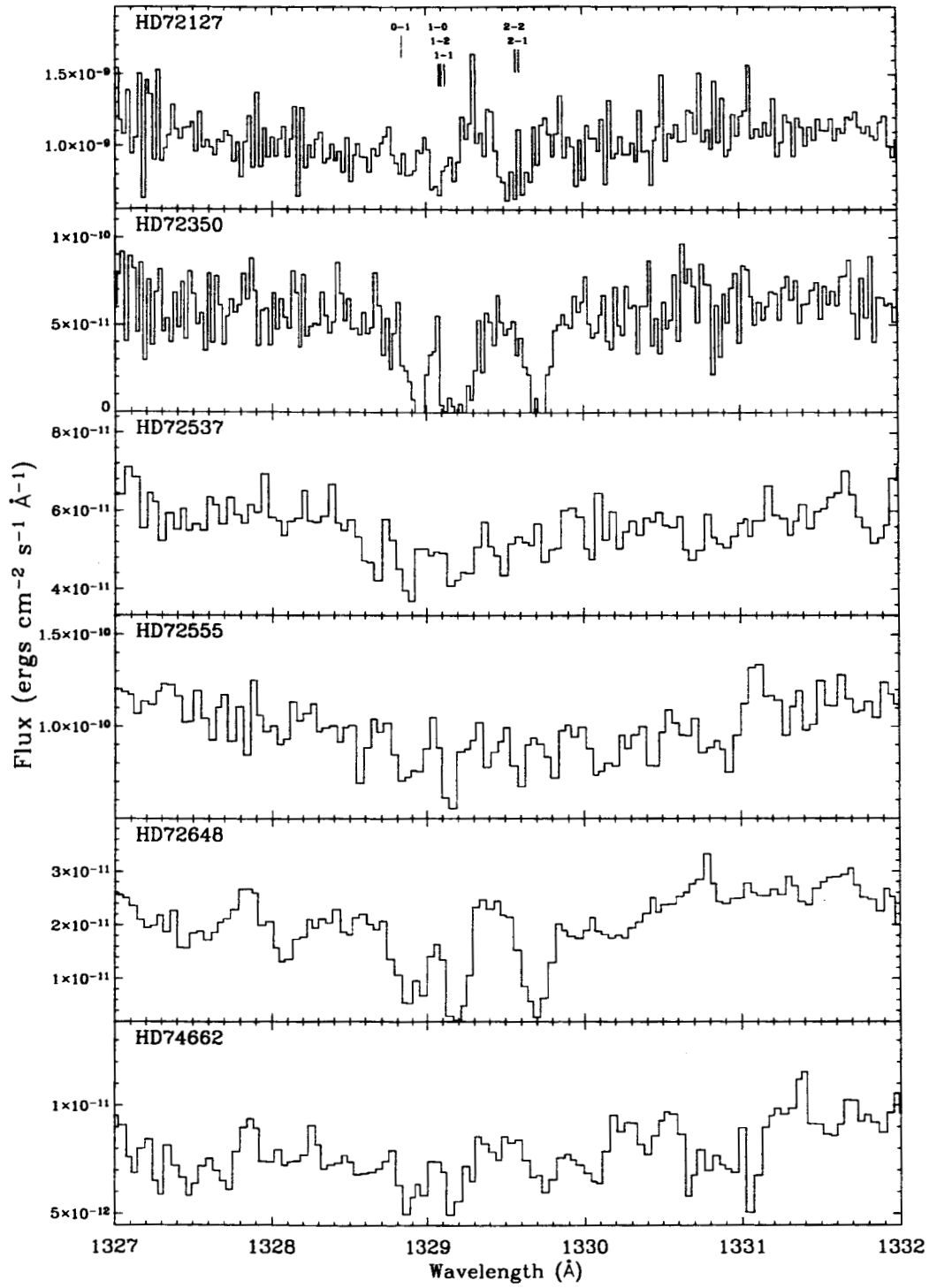
Fig. 3.— Montage of the spectral region near the 1392 Å C I multiplet in IUE high-resolution data (for the last six stars in our data set). The rest wavelengths of the transitions are indicated and labeled by the *J* values of the states.
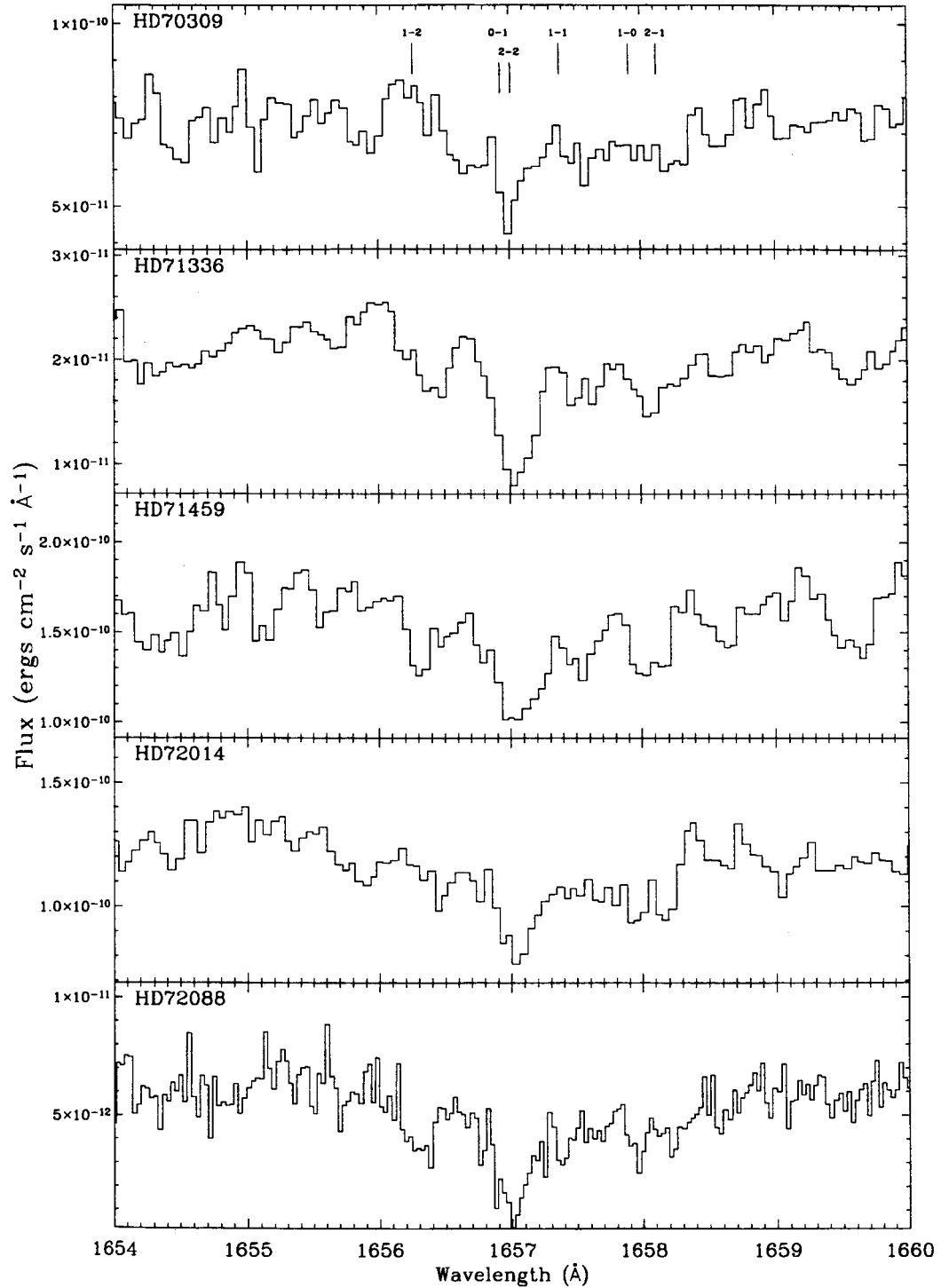
Fig. 4.— Montage of the spectral region near the 1657 Å C I multiplet in IUE high-resolution data (for the first five stars in our data set). The rest wavelengths of the transitions are indicated and labeled by the J values of the states.
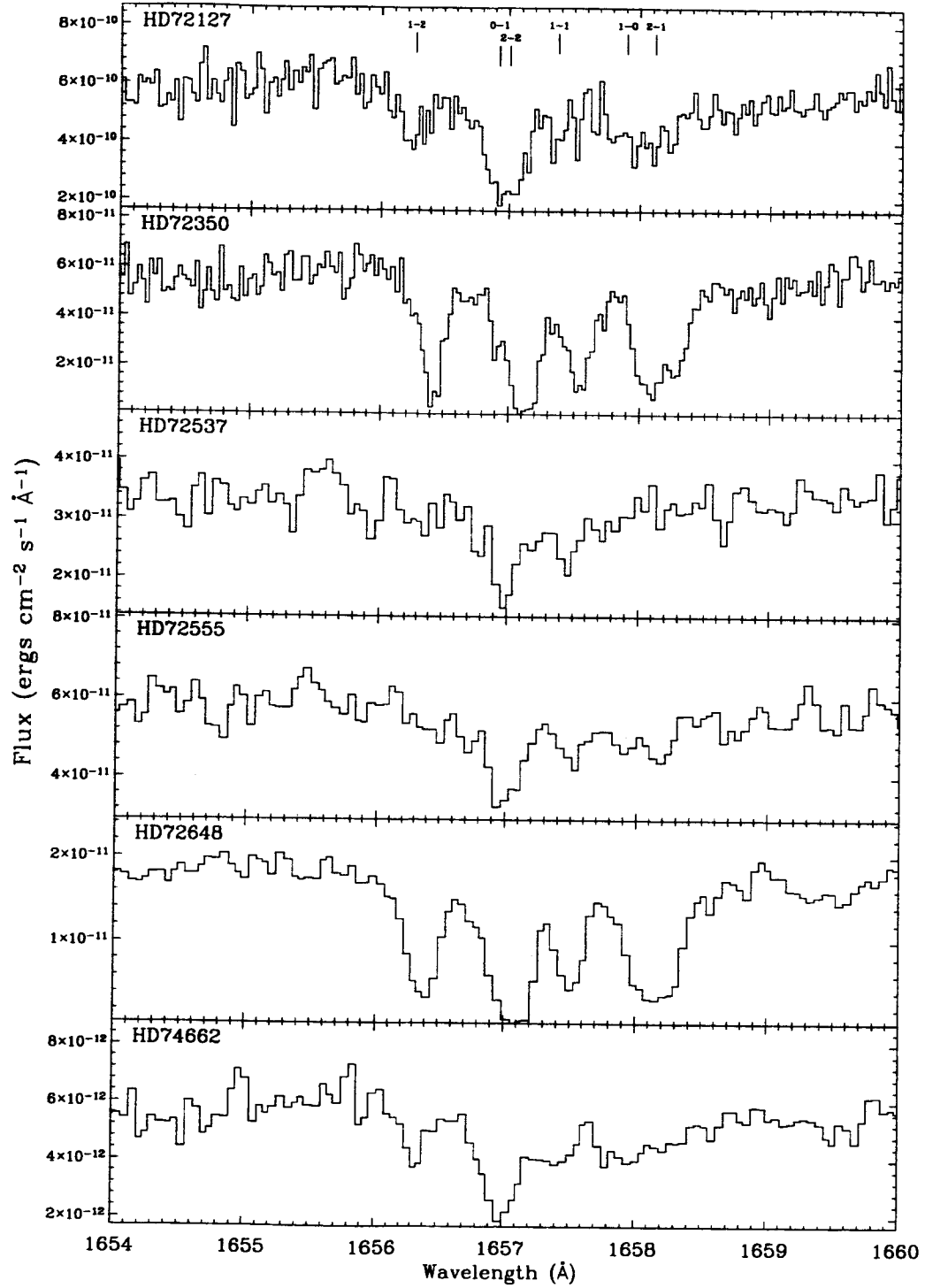
Fig. 5.— Montage of the spectral region near the 1657 Å C I multiplet in IUE high-resolution data (for the last six stars in our data set). A gaussian fit to the components is overplotted on the data.

Fig. 6.— Montage of the spectral region near the 1329 Å C I multiplet in IUE high-resolution data (for the first five stars in our data set). A gaussian fit to the components is overplotted on the data.

Fig. 7.— Montage of the spectral region near the 1657 Å C I multiplet in IUE high-resolution data (for the last six stars in our data set). A gaussian fit to the components is overplotted on the data.
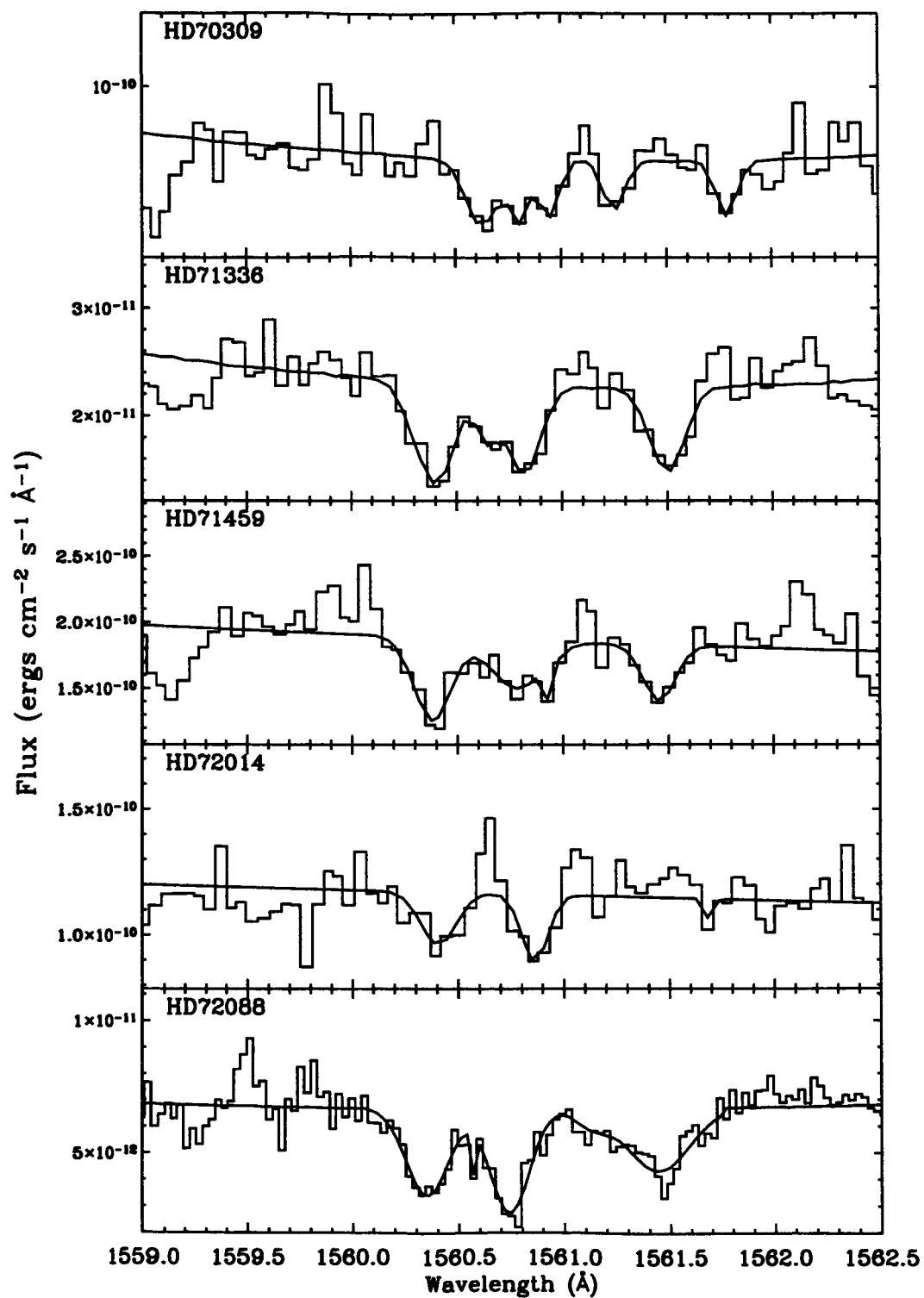
Fig. 8.— Montage of the spectral region near the 1657 Å C I multiplet in IUE high-resolution data (for the first five stars in our data set). A gaussian fit to the components is overplotted on the data.
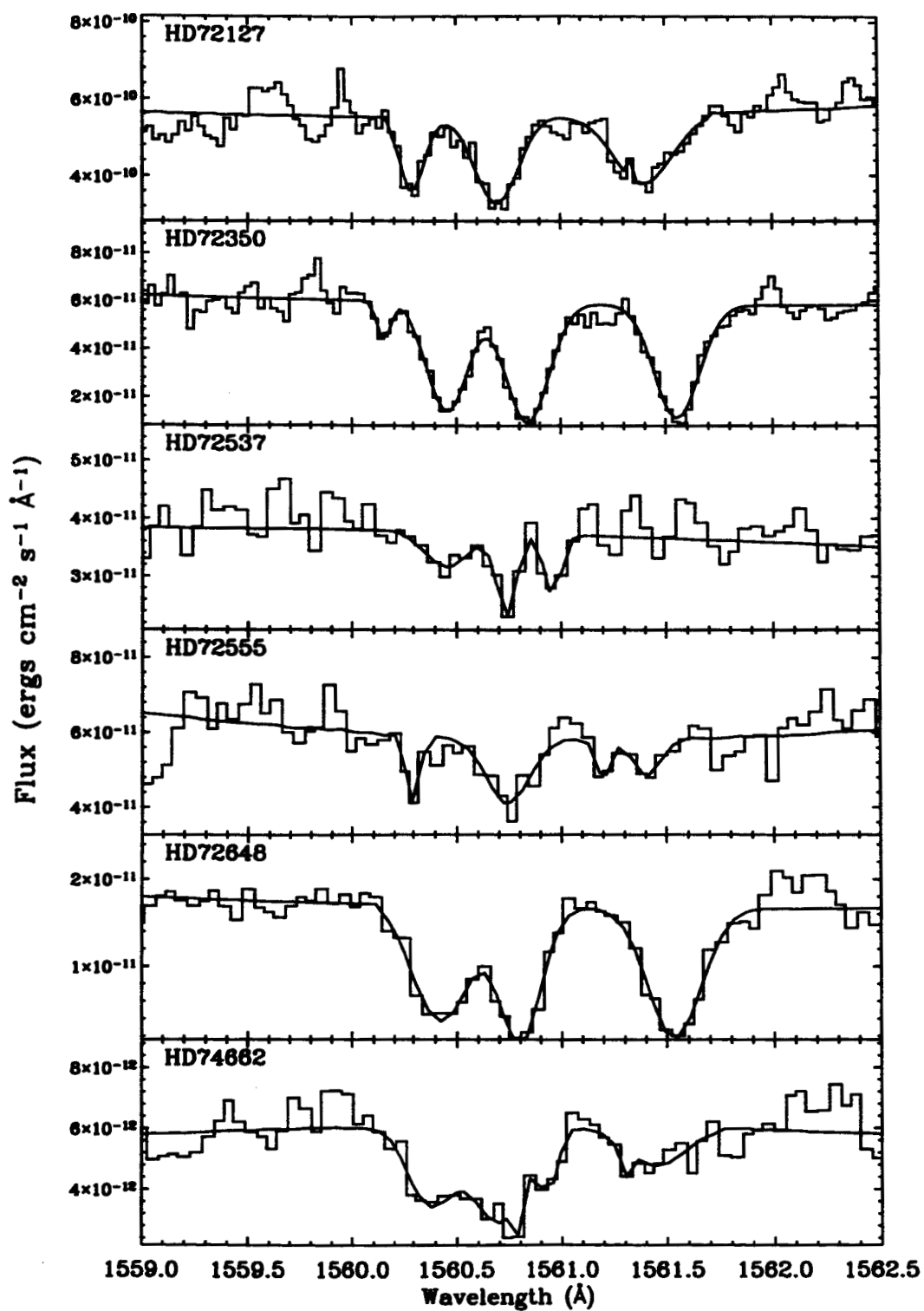
Fig. 9.— Montage of the spectral region near the 1657 Å C I multiplet in IUE high-resolution data (for the last six stars in our data set). A gaussian fit to the components is overplotted on the data.
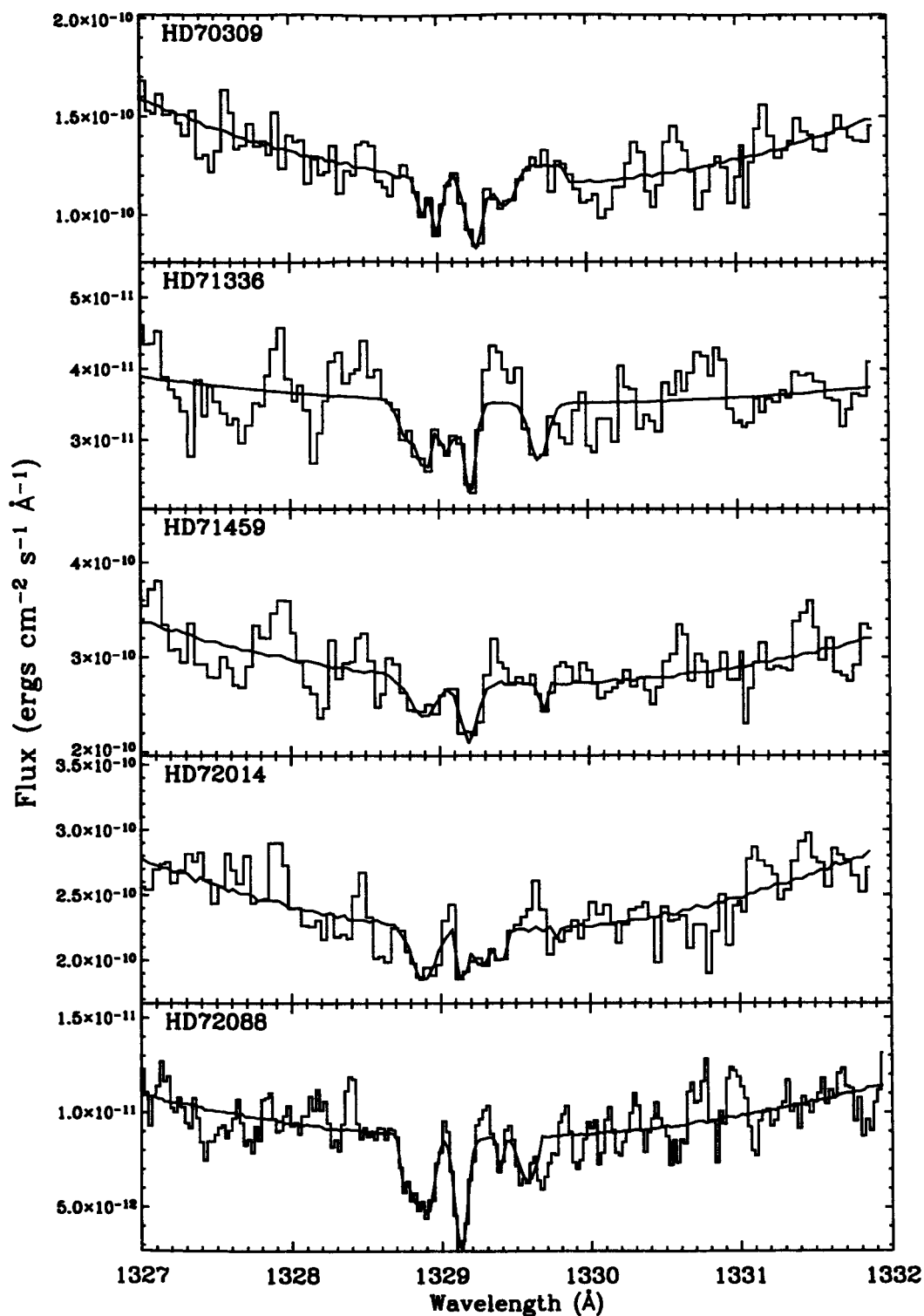
Fig. 10.— Montage of the spectral region near the 1657 Å C I multiplet in IUE high-resolution data (for the first five stars in our data set). A gaussian fit to the components is overplotted on the data.
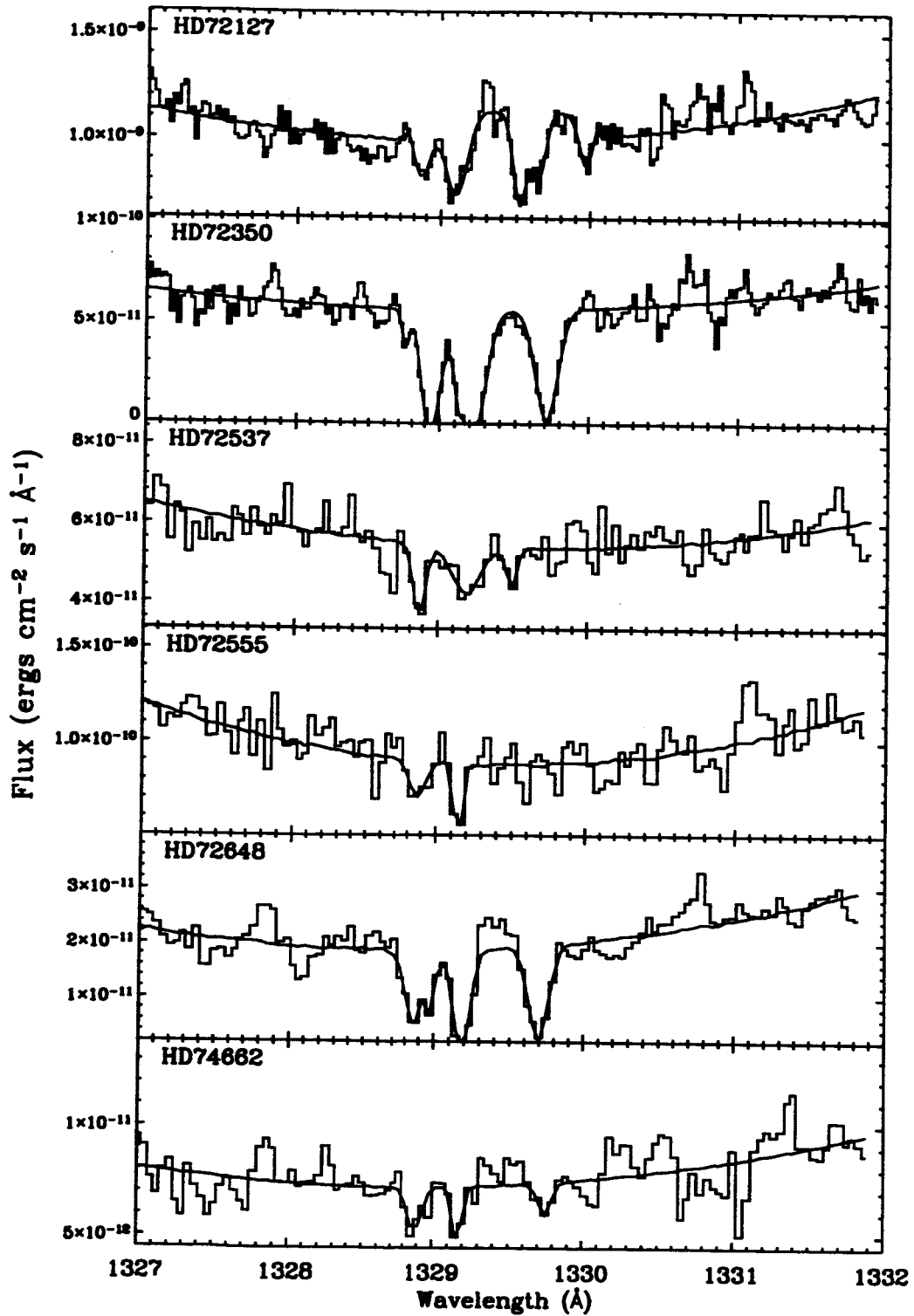
Fig. 11.— Montage of the spectral region near the 1657 Å C I multiplet in IUE high-resolution data (for the last six stars in our data set). A gaussian fit to the components is overplotted on the data.
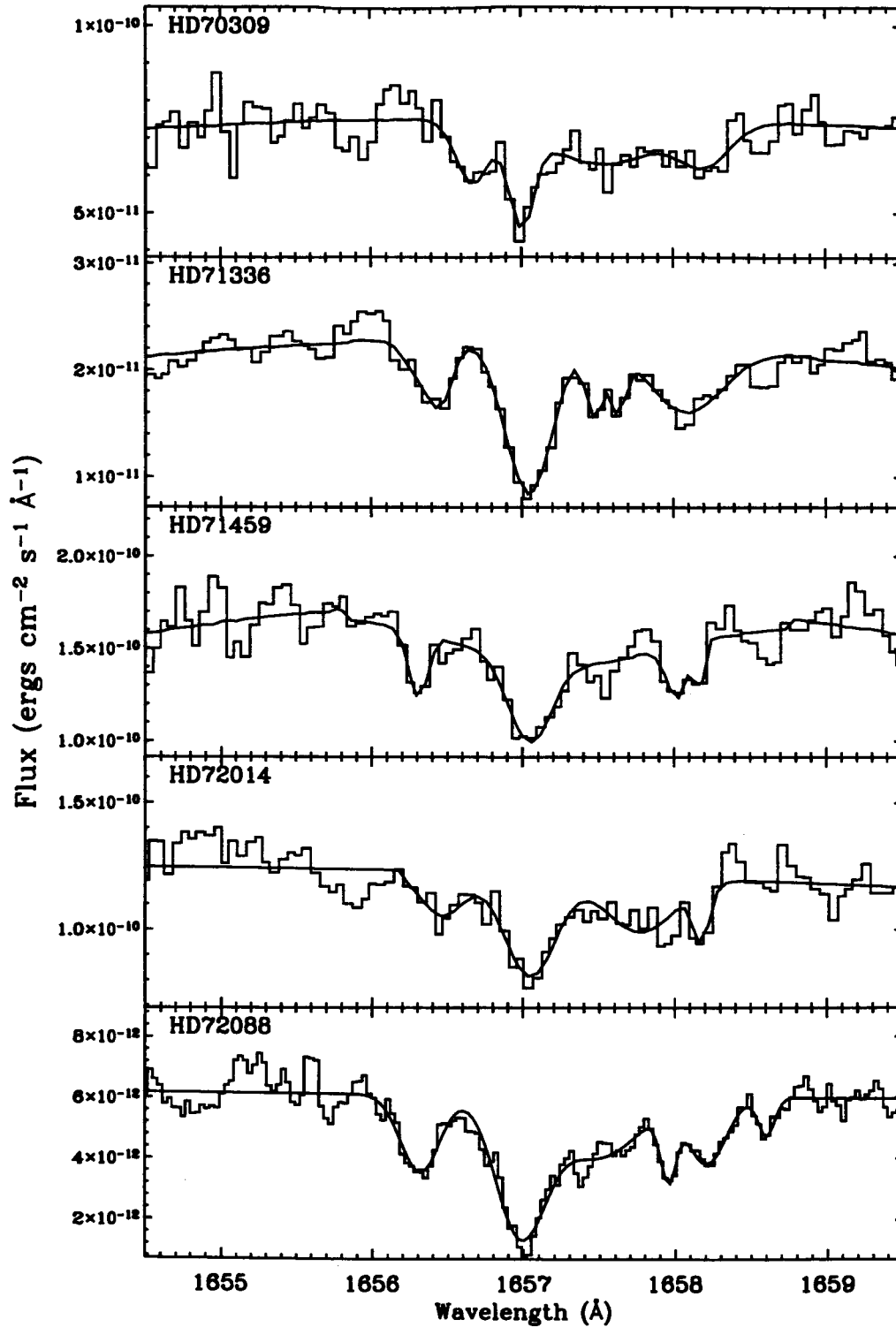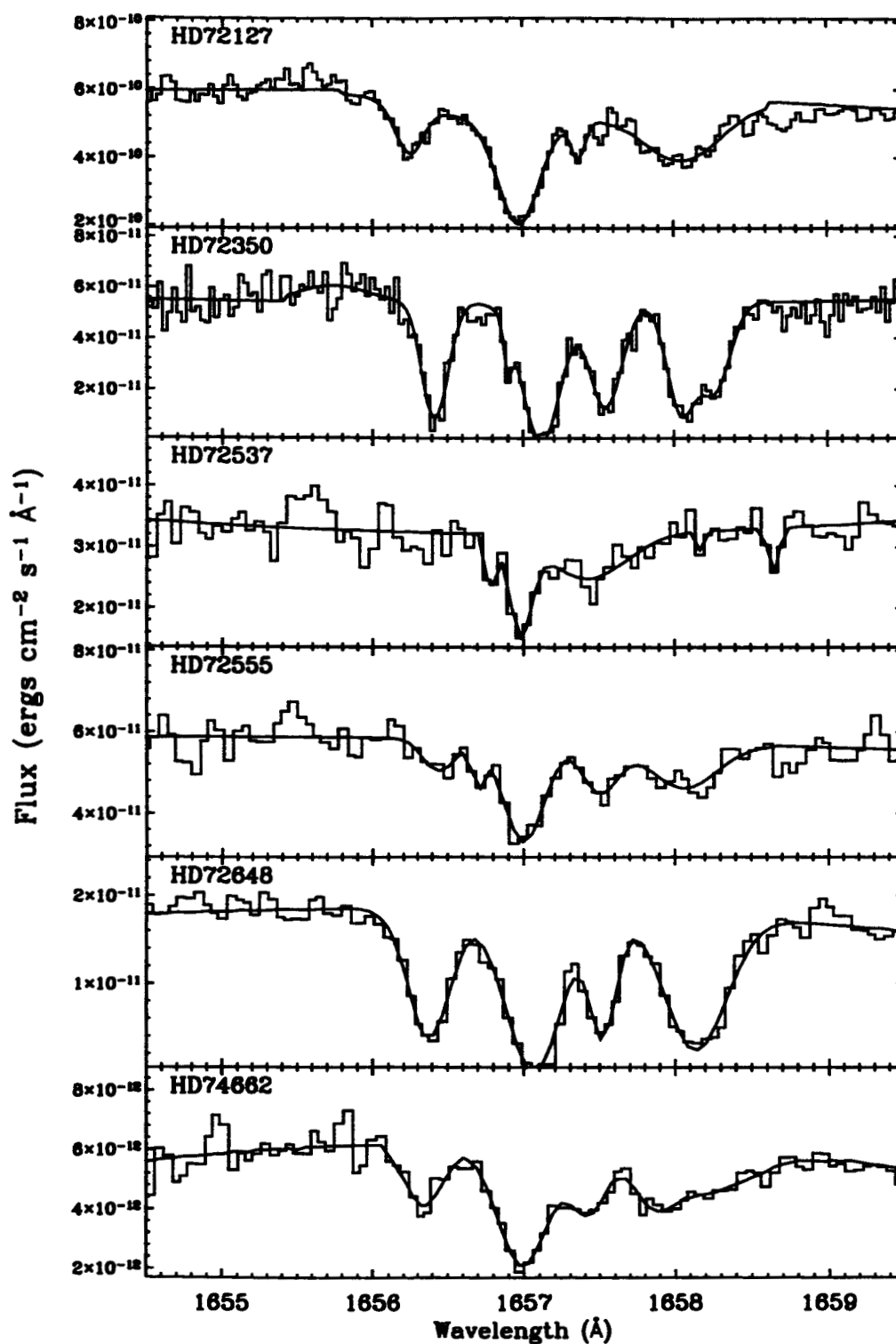
Table 3 lists the radial-velocity measurements of the C I lines for each of the 11 stars that showed strong high-excitation lines in one or more of the C I multiplets. The velocities have been corrected to heliocentric velocity by the IUESIPS software, or by hand for the early observations when the correction was not included in the software. The velocities were also corrected to LSR using a correction of 13 km s^{-1}. Note that the displacement of the high-excitation lines from the rest velocity of the ground state $J = 0$ component in each multiplet is generally consistent within the estimated errors with the expected displacement as tabulated in Table 2. Two exceptions are HD 71459 and HD 71336, where the high-excitation lines are broad and the velocity measurements must be considered less reliable. There is some indication from the line profiles that, at least in these two stars, the C I and C I* are blends of several higher velocity components, as Jenkins & Wallerstein (1995) found for HD 72089. The consistency between the expected wavelength and the observed wavelength of the C I* lines is sufficient for us to conclude that the strong lines we are seeing are indeed the high-excitation components. HD 72555 and HD 74662 have questionable results because the high-excitation gas was detected in only one of the four C I multiplets.

Within an individual spectrum, random errors in the velocity measurements are estimated to be ±5 km s^{-1}, based on repeated measurement of the same spectrum. Errors in the IUESIPS wavelength assignments, both systematic for the entire spectrum and internal consistency, are reported to be less than ±5 km s^{-1} (Smith 2001). However, image distortion due to temperature variations in the instrument can increase the errors for wavelengths near the edges of the SEC vidicon detector for some observations. In particular, the 1560 Å multiplet falls near the edge of the detector, and wavelength errors for this multiplet are estimated to be ±8 km s^{-1}. The other multiplets fall near the center of the detector and the systematic errors in the wavelength assignments are closer to ±5 km s^{-1}. Also, placement of the target in the large aperture can affect the accuracy of the wavelengths. The total random and systematic error is estimated to be ±8-10 km s^{-1}, with slightly larger values for lines near the edge of the detector. In the case of broad lines, the errors increase in proportion to the FWHM of the lines. For IUESIPS data, the equivalent width lower limit for reliable detection of an absorption feature is 25 mÅ (Nichols & Linsky 1996). Lines with equivalent widths below this limit are not reported.

Another source of uncertainty in this study is the non-uniform time epoch, which cannot currently be quantified. As Cha & Sembach (2000) have shown, the velocities and the equivalent widths of the interstellar line components in this region can vary on time scales of a few years (or less). While most of the spectra used in this study were taken during 1978-1979, a few were taken as late as the mid-1990's.

It is certainly possible that there are high-velocity components blended in these lines,

as Jenkins and co-authors found in the case of HD 72089, but we cannot confirm this on the basis of IUE resolution. We can confirm that the C I* is unusually strong for these 11 stars, compared to 42 other lines of sight through the Vela SNR.

2.2. IRAS data

IRAS data for the entire region of the Vela SNR were processed with the HIRES software specifically for this project by the IPAC staff. The HIRES algorithm uses a Maximum Correlation Method (Aumann et al. 1990) described at

http://irsa.ipac.caltech.edu/IRASdocs/hires_proc.html

The IRAS raw survey scans were first combined into an 8° × 8° field. Destriping and flat background removal were done with this large image. A flux bias value determined for each leg of the scan was added to the pixel values at this point to accommodate the positive input value constraint of the HIRES processing. The large image was then divided into subimages of 512 × 512 pixels and processed separately through the HIRES algorithm. The resulting images were recombined into the larger field and the arbitrary bias was then subtracted out of the data. There are some pixels in the final images with small negative values within the noise level. We have set these small negative values to zero. The images of the 4 bandpasses were created using 20 iterations of the HIRES code. Flux accuracy is assumed to be ∼20%. However, there may be a systematic error in the absolute value of the flux for each of the 4 bandpasses. The arbitrary bias that is used in the HIRES process to scale the data for processing may have resulted in negative flux values for pixels that are not within the noise level. A correction for this arbitrary bias will need to be considered before maps of the 60/100μm ratio can be quantitatively analyzed. This correction has not been derived for this paper.

A three color image of the HIRES IRAS data is shown in Figure 6, with ROSAT X-ray contours superimposed on the image. We have excluded the 60μm band in this image because of the possibility of [O I] emission in that band. The image in Figure 6 was constructed with blue for the 12μm band, green for the 25μm band, and red for the 100μm band, and scaled in intensity to bring up the fainter emission. Where all three bands are approximately equally bright, the colors combine to display as white. There are small instrumental artifacts in the image identifiable as crosses or short streaks.
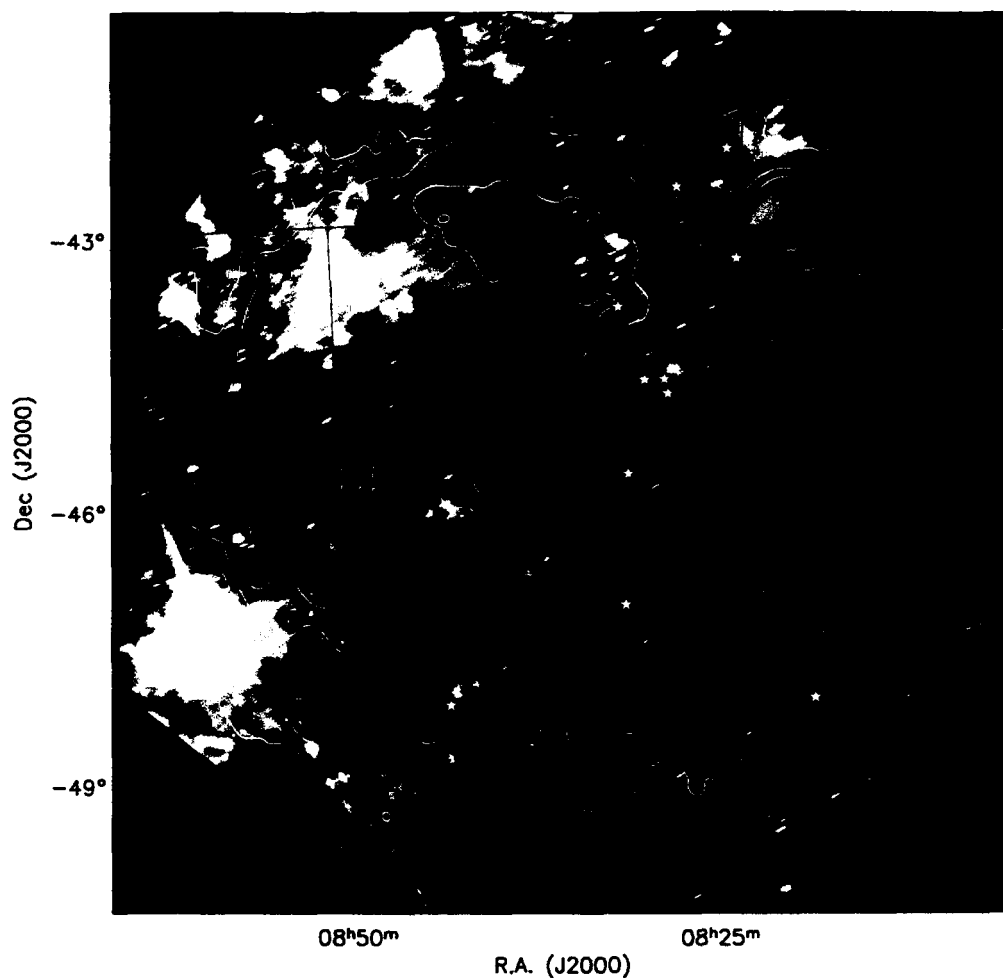
Fig. 11.— Three color image of IRAS HIRES data. Blue represents the 12μm band, green the 25μm band, and red the 100μm band. The data were scaled in intensity to bring up the faint emission. Contours are soft X-ray emission from the ROSAT All Sky Survey (Aschenbach 1998). Stars plotted are the stars identified as showing strong C I*.

3. Discussion

3.1. Strong High-Excitation C I*

A spatial plot of the stars in Table 3 is shown in Figure 7, superimposed on the ROSAT image of the Vela SNR (Aschenbach 1998). All eleven stars in Table 3 have distance estimates of at least 250 pc, so they are expected to be background to the Vela supernova remnant. The stars that show such excited state C I* in their spectra are spatially related in that they form a narrow "band" running north (near Pup A) to south along, but inside of, the western edge of the X-ray bright region of the SNR. The two exceptions are HD 74662 and HD 70309 on the southern edge of the supernova shell. This band is about 1° wide on the image, which is 4.4 pc using a distance to the Vela SNR of 250 pc. It extends about 20 pc from north to south. The band appears confined to a narrow region, suggesting it is not pervasive in the supernova shell but perhaps is due to dense, pre-existing clouds in the SNR that are interacting with the shock. The band of strong C I* lies close to the sharp line in the ROSAT X-ray image separating the high surface brightness region and the low surface brightness region, suggested by Seward (1988) and revealed with ROSAT. However, the strong C I* band lies just inside the high X-ray surface brightness region. This morphology suggests there is a relationship between the C I* band and the low X-ray surface brightness region to the west.
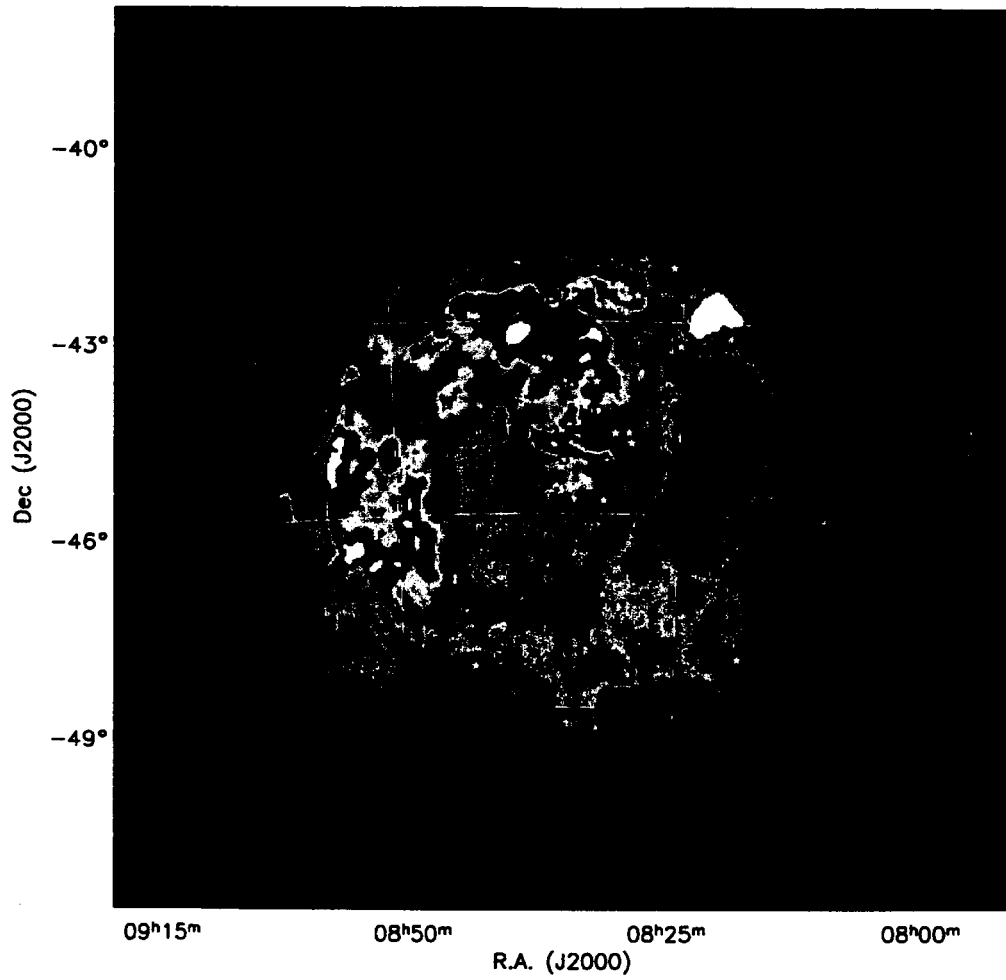
Fig. 12.— ROSAT all-sky survey image of the Vela SNR for photon energies $0.1 < E < 2.4$ keV with the stars that show strong high-excitation C I absorption overplotted.

HD 72648 and HD 72350 clearly have the strongest C I and C I* lines of the 11 stars. These two lines of sight are separated by about 3 pc at a distance of 250 pc. There is considerable variation in the strength of the C I* lines among the eleven stars, although the lines of sight, with the exception of HD 74662 and HD 70309, lie within the narrow band as described above and some of the lines of sight are separated by less than 2 pc (d=250 pc). The variation in the strength of the C I* among the 11 stars suggests multiple dense clouds in close proximity rather than a single large cloud.

Jenkins & Wallerstein (1995) observed HD 72089, which lies $\sim$45' south of HD 72088, with GHRS on HST, measuring the components of the C I lines 1656Å, 1329Å, and 1280Å. They found evidence of 6 high-velocity components in the line of sight to HD 72089 in the excited state transitions as well as the ground state for C I, with radial velocities of 1, 9, 15, 27, 85, and 121.5 km s^{-1}. The high-velocity components at +85 km s^{-1} and +121.5 km s^{-1} have remarkably large column densities of 1.0 $\times$ 10^{13} and 5.5 $\times$ 10^{13}, respectively. These large column densities imply a very high compression in the gas in order to populate the C I* to this extent. These authors calculate a dynamical pressure of $2 - 4 \times 10^{-9}$ dyn cm^{-2}, and conclude that the origin of the C I* is the a surface of a dense cloud after the passage of the shock, suggesting that the dense cloud is a molecular cloud engulfed by the SNR. The fact that only positive velocities are found in the C I data indicates the dense clouds are receding and probably on the back side of the SNR. We did not identify unusually strong C I* in the IUE spectrum of HD 72089, because the strength of the C I* lines was not large enough to meet our selection criterion. Note, however, that we only examined one early IUE spectrum of this star, taken 13 years before the HST spectrum with GHRS reported by Jenkins & Wallerstein (1995). This star lies within the narrow band containing the positions of the stars for which we have also detected unusually strong C I*.

Wallerstein et al. (1995) observed HD 72127A and HD 72127B with GHRS and also found strong C I* toward these stars, as well as two high-velocity components in the members of the multiplets. However, the situation was not identical to that of HD 72089 in that the very high pressure estimates were not associated with high-velocity features, but rather with the main velocity components.

Our measurements show that the C I* lines for the 11 stars listed in Table 1 are much stronger than would be expected along a line of sight of unperturbed ISM. They are also stronger than the C I* lines in the other 42 Vela stars we studied. The interpretation of the strong high-excitation features we have detected is guided by the definitive work of Jenkins using GHRS and STIS identifying the high-velocity features in the spectrum of HD 72089 as due to several velocity components in each member of the multiplet. With IUE, we cannot identify high-velocity features for individual members of the C I multiplets. It is plausible

that the strong components we have detected also include multiple high-velocity components, as in HD 72089. Unfortunately, higher resolution data for C I* do not exist for the any of the 11 stars we identified as having unusually strong C I* in their lines of sight.

We did not make any determinations of column density from the IUE results, due to the strong possibility that these lines are composed of multiple blended velocity components. Therefore we do not have quantitative results of pressure and density in this region. The fact that we did not identify strong C I* toward HD 72089 because the high-excitation line did not meet our criterion of 30% flux minimum of the ground state component implies the 11 stars we did identify in Table 3 represent very high pressure and density, at least as high as that determined by Jenkins & Wallerstein (1995) for HD 72089.

In our analysis of the spectra of all 53 spectra of stars behind the Vela SNR, we also found a systematic red-shift of many ground state C I components in each multiplet, compared to other neutral species such as Si I and Cl I. For each of the 53 spectra in this study, we measured the radial velocity of the ground state $J=0$ component of each multiplet. Twenty-two of the stars in our sample were found to have ground state C I at a positive velocity of 8-26 km s^{-1} with respect to the other neutral ions. The average velocity of the $J=0$ line for the four C I multiplets in each spectrum are listed in Table 4. The average velocity displacement for these components among all the stars in this table is $\sim+20$ km s^{-1}. However, the Si I and Cl I lines are generally at zero velocity in the LSR velocity frame in these spectra, so we conclude that the ground state C I lines are probably a blend of the zero velocity component that would be expected along the intervening line of sight, and a higher velocity component associated with the Vela SNR. Higher resolution spectral data will be needed to confirm these multiple low velocity C I components. We were in fact able to identify 2 components in the ground state C I in the spectrum of HD 72088 (+12 and +26 km s^{-1}).

Dubner et al. (1998) find an H I shell around the Vela SNR, closely following the outer X-ray-bright shell as seen in ROSAT data (but excluding the X-ray dim western segment). The H I shell is expanding at about 30 km s^{-1}, and believed by Dubner et al. to encase the backside of the supernova remnant shell. The ground state C I may be associated with the H I shell, which is probably the recombined post-shock shell behind the shock front. At the locations of the stars for which we detected very strong C I*, Dubner et al. (1998) find localized enhanced H I emission in the velocity ranges +30 and +105 km s^{-1}, with a band width of 6.6 km s^{-1}. These two velocity ranges are very similar to the velocity displacements seen in C I lines in this study, and to the high-velocity components seen by Jenkins & Wallerstein (1995) in HD 72089.

3.2. Infrared Temperature Map

The HIRES processing of the Vela SNR contains considerable new information, much of which is beyond the scope of this paper. Our focus is on identifying dust emission that can possibly be associated with the Vela SNR, particularly in the region where we have found very strong C I*. One of the most striking features of the image in Figure 6 is the clear discontinuity of dust emission between the interior of the SNR and the exterior in the southern hemisphere of the SNR. We believe this is the first time the thick dust shell surrounding the hot gas interior of the Vela SNR has been detected. The size of the dust shell is apparently smaller than the X-ray emission region, implying the possibility of an X-ray halo.

In Figure 6, the pervasive IR emission from the Vela Molecular Ridge (VMR) above approximately $b_{II}=-1°$ is present in the northern portion of the Vela SNR. The VMR is a complex of 4 giant molecular clouds at an approximate distance of 700 pc, with boundaries approximately defined by: ra=8h44m,dec=-39d00m (north point); ra=8h28m,dec -42d00m (west point); ra=9h16m,dec=-52d00m (south point); and ra=9h32m,dec=-49d00m (east point), Another IR structure in the line of sight to the Vela SNR that could confuse the results of our analysis is the IRAS Vela Shell, a wind and supernova blown bubble surrounding the association Vel OB2, partially overlapping the Vela SNR in line of sight. However, the Vel OB2 association is believed to be at about 400 pc distance, considerably more distant than current estimates for the Vela SNR. Some of the hot dust in the line of sight to the Vela SNR might be due to the Vela IRAS Shell.

However, an anti-correlation between the X-ray and IR emission in the Vela SNR line of sight is suggested by the data. The bright structure in the northeast seen in white and green corresponds to reduced X-ray emission in this region. At least some part of this bright IR emission may be internal to or foreground to the SNR, absorbing the X-rays in this region. The SNR, Pup A, less than 1° in diameter in the northwest corner, appears as primarily green in this image, and is background to the Vela SNR.

The bright X-ray projection known as Bullet D on the eastern rim of the SNR is in a region of low IR emission. Slightly interior to Bullet D is a large bright X-ray region, which traces fairly closely a region of low IR emission. An nearby interior region of lower X-ray emission (approximately 8h 52m, -44°to -45°) corresponds to relatively strong (red in the figure) 100μm emission. In the southeast, along the rim of the SNR, the irregular morphology of the X-ray emission is generally traced with very low IR emission. Thus, in the east and southeast, there is a substantial anti-correlation between the X-ray emission and the IR emission.

In the west, the outermost rim of the SNR is seen well defined in Figure 6 by the discontinuity between low IR emission interior to the SNR and the cool and hot dust exterior to the SNR, which closely follows the faint X-ray rim seen in the ROSAT data. However, there are exceptions to the anti-correlation between X-ray emission and IR emission in the southwestern portion of the SNR. There is a distinctive feature in the southern hemisphere that appears as a narrow "pillar" in the southwestern region, superimposed on the shell interior, from approximately 8h 38m, 47d 30m to 8h 28m, 45d 30m. The "pillar" of IR emission, which is primarily 100μm emission in Figure 6, is not coincident, below -46° declination, with the bright inner X-ray discontinuity, which demarks the transition from the X-ray bright to the X-ray dim portions of the SNR. Also, along the southeastern rim of the SNR, an irregularly shaped X-ray bright protrusion is not matched with a similarly shaped IR-dim region. This X-ray protrusion at 8h 35m, -48.5° is the one notable exception to the nearly complete anti-correlation between X-ray and IR emission along the Vela SNR rim for the entire southern hemisphere of the SNR.

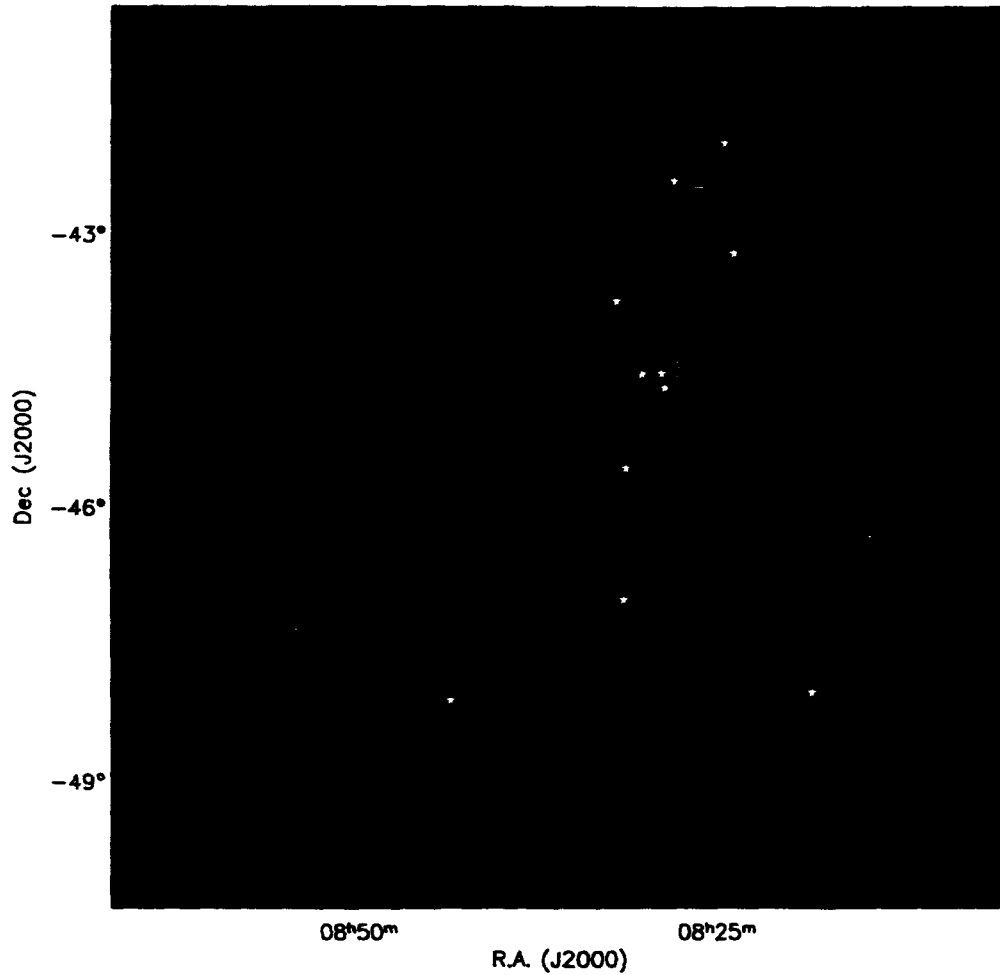Fig. 13.— Temperature map of the Vela SNR created using a two component fit to the IRAS HIRES data on a pixel-by-pixel basis. This two-color image shows the cool temperature component represented as red and the hot temperature component represented as blue. Only IRAS emission inside the X-ray contour was included in the temperature calculations. The numbered areas indicate regions where the temperature values are reported in Table 5.

Using the HIRES images of the four IRAS bands, we created a temperature map of the dust, following the method of Saken et al. (1992) in calculating a two component temperature fit for each pixel. Black body emissivity of the grains is assumed, modified by an emissivity law, $(\lambda_0/\lambda)^{1.5}$ where $\lambda_0 = 0.2\mu m$, First, the IRAS fluxes for the four bands ($i = 12, 25, 60, 100\mu m$) were calculated for each pixel as follows:

$$F_i = b_1 \int B_\lambda(T_1)(\lambda_0/\lambda)^{1.5} R_i(\lambda) d\lambda + b_2 \int B_\lambda(T_2)(\lambda_0/\lambda)^{1.5} R_i(\lambda) d\lambda.$$

where B_λ is the Planck function, $R_i(\lambda)$ is the response function of the IRAS detectors, T_1 is the hot dust component temperature, and T_2 is the cold dust component temperature. A factor of π is included in the constants b_i. These fluxes were fit to the observed fluxes to determine b_1 and b_2, and the temperatures for the 2 components, T_1 and T_2.

The results of this thermal dust modeling are shown in Figure 8. For each pixel in Figure 6 inside the ROSAT X-ray outermost contour, the hot component of the dust is coded as blue and the cool component is coded as red. Only pixels inside the X-ray perimeter as defined by the outermost contour were included in the modeling, so pixels outside the X-ray perimeter in Figure 8 contain no temperature information. Any error in the arbitrary bias value applied to the HIRES images during processing will change the absolute values of the temperature determined, but not the pixel-to-pixel relative variations. This temperature map reveals interesting information for several regions of the Vela SNR.

The southern rim of the SNR is clearly seen as a sharp edge between the warm dust in the swept-up ISM and the hot interior of the SNR devoid of warm dust. This clearly defined shell continues on the western rim of the supernova remnant, outlining the western X-ray shell seen rather faintly in ROSAT data. The southern rim of the SNR is clearly defined, with the dust shell of swept-up material primarily at low temperatures. An obvious exception is the rim at the location of Bullet D. The dust appears to follow the X-ray protrusion in the rim at this location, and the dust is much warmer (blue) and spatially very narrow. The outermost western rim of the dust shell also shows higher temperatures than other parts of the rim of the SNR.

In the north, the IR emission may contain contributions from the Vela SNR, VMR, and possibly other foreground or background objects. However, some of the hot dust is clearly anti-correlated with X-ray emission. The large X-ray bright region centered at approximately 8h 37m, -43° is apparently outlined by a region of hot dust in the northeast, north, and east. This hot dust seems to imply that some of the IR emission in the north is due to dust associated with the Vela SNR that is undergoing shock processing.

The spatial anti-correlation between X-ray and IR emission that we have described is expected for a shock propagating through a dusty medium. Vancura et al. (1994) modeled the grain evolution and emissivity behind non-radiative shocks. By including consideration of grain sputtering, heating, and decelerations in the post-shock flow, they were able to predict the X-ray/IR emission ratio for various swept-up columns of N_H and for several shock velocities, although the lowest shock velocity they considered was 300 km s^{-1}. Initially after shock passage, the grains are heated, raising the IR emissivity and in particular the 60/100 μm ratio. This stage corresponds to the high dust temperature regions in Figure 8. However, as grain mass is reduced by sputtering, X-ray emission increases due to increased metallicity of the gas, resulting in a higher X-ray/IR ratio. This stage is correlated with the high X-ray emissivity regions. So the spatial anti-correlation of the X-ray/IR emissivity is expected as a result of the grain evolution after shock passage.

All of the 11 stars identified in Section 2 lie in the line of sight to hot dust regions. As noted, the three most northerly stars are in the line of sight to the VMR (d=700 pc), but are believed to be foreground to that structure. The strongest high-excitation C I was found in HD 72648 and HD 72350, which lie near relatively strong 100μm emission. In fact, all 11 of the stars for which we identified strong high-excitation C I lie near or superimposed on 100μm emission, except for HD 72555.

Six small regions were selected in the color map to quantify the calculated temperatures. These regions are indicated on Figure 8 and tabulated in Table 5. Plots of the temperature fits for these 6 regions are shown in Figure 9. Five of the six regions are well fit with a two-temperature model. Only the region selected on the southwest pillar noted above is best fit with a single temperature component (70 K). The low temperature would appear to preclude the interaction of this feature with the SNR, in spite of the suggestive morphology. Region 3, which includes the lines of sight to three of our stars with strong C I* has a relatively high hot temperature component of 223 K, and also a relatively high low temperature component of 25 K. The highest dust temperature estimate of 265 K is found in the protrusion near Bullet D. Region 4, lying just north of strong X-ray emission, also shows a high hot component in the dust of 242 K.

In summary, the temperature map suggests that much of the IR emission in the direction of the Vela SNR can be directly associated with the SNR in the sense that dust is interacting with the shock and hot gas in the interior of the SNR. Certainly some of the IR emission may be either foreground or background, but we argue that the hot dust, with calculated temperatures above 200 K for the hot component, is dust interior to or impacted by the SNR. Specifically, the hot dust as portrayed by blue in Figure 8 tends to outline and be anti-correlated with the strongest X-ray emission. The hot dust is, however, strongly correlated
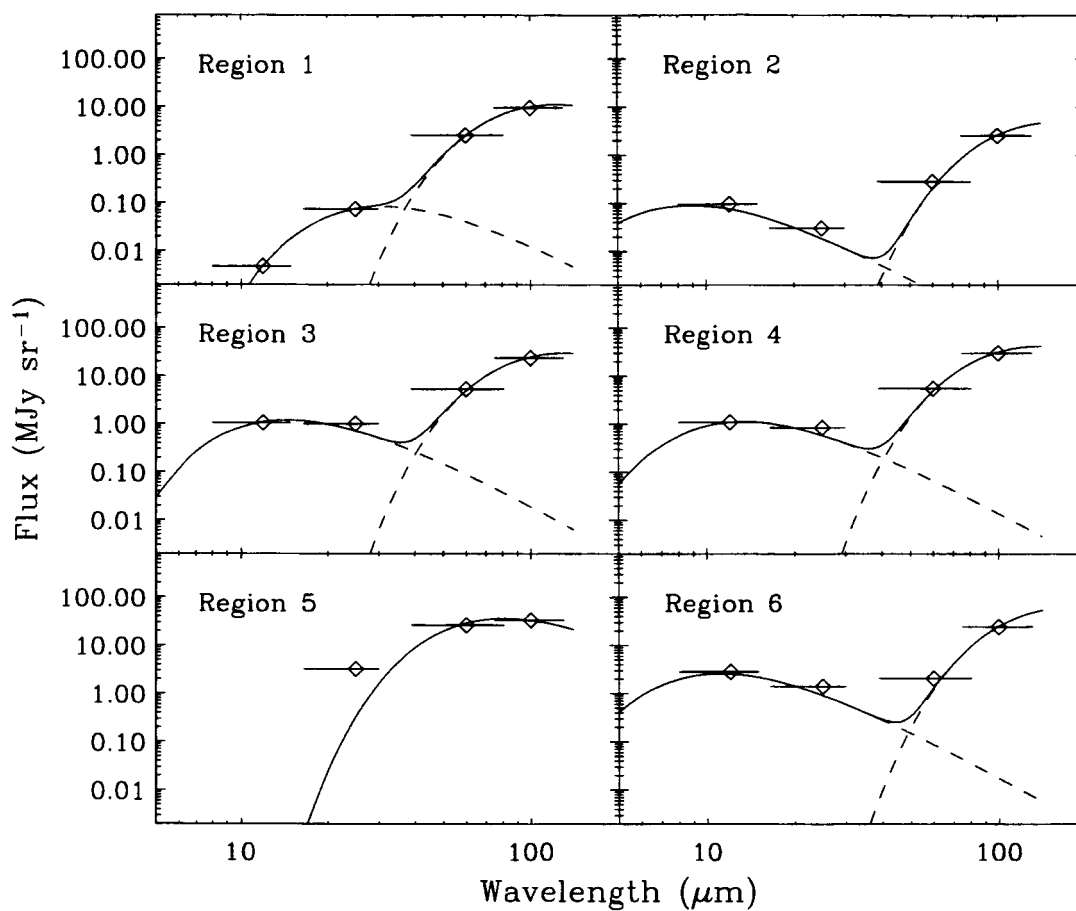
Fig. 14.— Temperature model fits to the IR data in regions 1-6, as indicated in Figure 8. In addition to the data points for the 4 IRAS bandpasses, a line showing the width of the band at the 90/response level is shown. A two-component temperature fit was satisfactory for all regions except region 5.

with optical emission filaments. The implication is that the hot dust toward the Vela SNR is in fact related to that SNR and can be interpreted as the result of shock processing in a dusty medium within or immediately surrounding the SNR. The lines of sight to the stars for which we have detected strong C I* tend to lie in regions of hot dust, consistent with an interpretation that this strong C I* is produced in high pressure, high density regions with large dust populations.

3.3. Optical Filaments

Optical filamentary structure has been interpreted as originating in cooling gas behind shocks that have been slowed due to dense clouds, creating a high density, high compression region behind the shock (Fesen et al. 1982). The regions near the band of stars showing strong C I* in their spectra are particularly rich in optical filaments, both Hα and O [III] (Parker et al. 1979). We have mapped the stars with strong C I* on the optical DSS image in Figure 9. The DSS image is a broadband image centered at 4500/AA/ with a FWHM of 1500/AA. Emission lines of [O III] at 5007/AA/ and at 4363/AA, H/*beta* at 4681/AA, H/*gamma* at 4340/AA, [Ne III] at 3869/AA, [S II] at 4070/AA, and [Fe III] at 4658/AA/ are included in this bandpass. The lines of sight to the 11 stars in the band tend to intersect the optical filamentary structure. The optical filaments include overlapping rings or nearly complete arcs of emission, reinforcing the idea that these clouds are engulfed in the SNR. If these rings and arcs represent the surface of the clouds, we find the physical size of these clouds to be 1-4 pc in diameter, assuming a distance of 250 pc. In addition to the arcs and rings of optical emission, there is filamentary and clumpy emission throughout this region, suggesting cloud intersections and possibly a mix of much smaller cloud sizes.
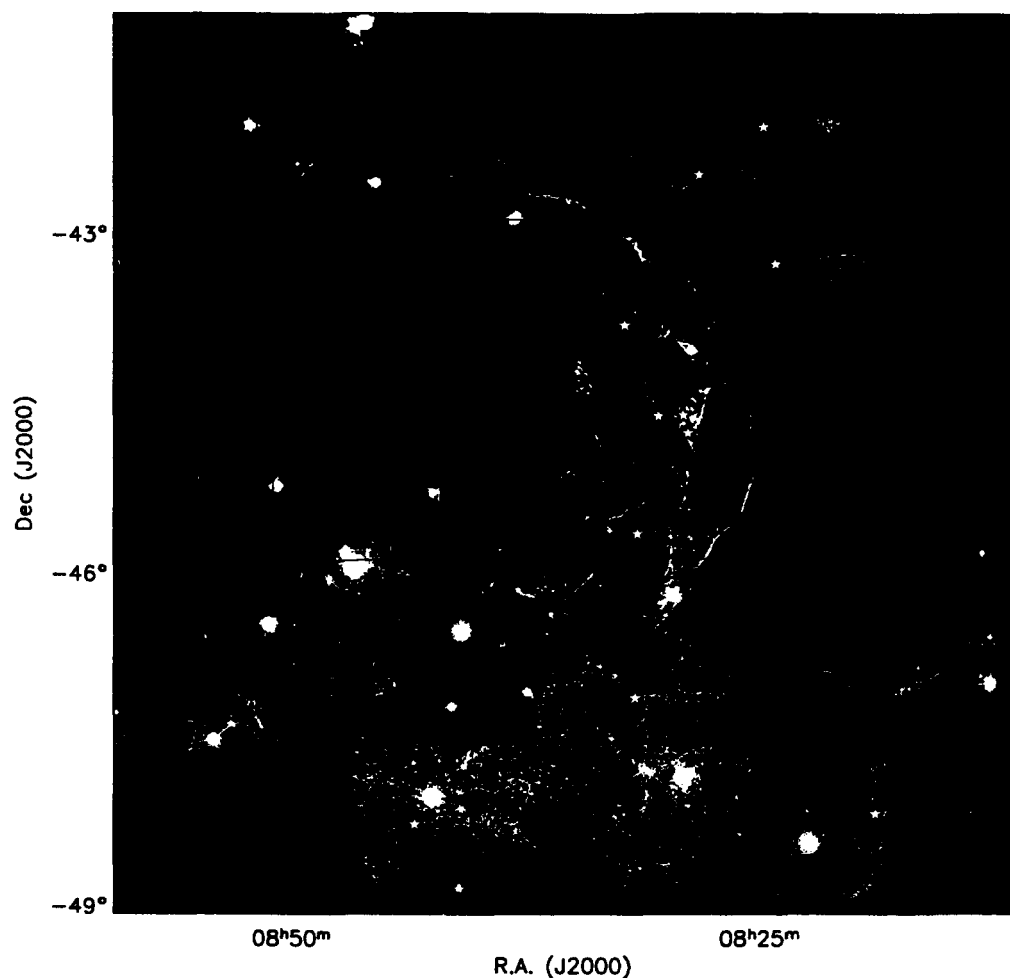
Fig. 15.— Digital Sky Survey mosaic of the Vela SNR with the strong high-excitation C I stars overplotted. Most point sources have been removed via filtering. The emission is scaled logarithmically and truncated at the high and low values to bring out the filamentary diffuse emission from the SNR shocks.

The optical filaments could have another origin than clouds interacting with the supernova shock wave, such as a remnant of a precursor-generated structure, a cocoon or torus associated with the pulsar, or the signature of face-on bullets impacting the SNR shell.

3.4. X-ray Emission

The western region of the Vela SNR shows a lower X-ray emission compared to the rest of the SNR (Seward 1988) (see Figure 7). The outer rim of the SNR in the western region is faintly visible in the ROSAT data. The X-ray flux does not decrease gradually toward the west, but rather shows a clear discontinuity along a projected line starting at approximately 8h 25m, -43° 00′ continuing south to -45° 00′ then southeast to 8h 30m, -47° 00′. Our discovery of a band of strong high-excitation C I near this discontinuity, coupled with the spatial location of hot dust and optical filamentary structure strongly suggests that the discontinuity in X-ray flux may be a consequence of the SNR evolution, rather than a foreground absorption. If the X-ray dim western region were the result of foreground absorption, it would be a remarkable coincidence in alignment with the band of strong C I* and the presumed associated dense clouds. However, a blowout of the SNR in the southwest might also be a plausible explanation for the low X-ray flux in the western portion of the SNR.

When the SNR blast wave encounters dense clouds, it will decelerate as it moves through them. If the dense clouds are numerous and closely spaced, the outer shell of the SNR will be distorted from spherical symmetry, as in W28 (Rho & Borkowski 2002). An important signature of a shock wave encountering dense clouds would be the reverse shock, which would enhance and harden the X-rays behind the shock front due to the higher temperatures. Comparatively harder X-rays were in fact found near the western X-ray bright/dim discontinuity by Kahn et al. (1985) and Lu & Aschenbach (2000), supporting a scenario of shocked dense clouds producing reverse shocks in this region of the Vela SNR. Other regions of the SNR, aside from the pulsar region, exhibit softer X-rays.

The Vela SNR does not exhibit uniform central brightness, as some centrally brightened SNRs, such as W28, W44, IC 443, and CTB 109, but there are regions of diffuse bright X-rays now seen as anti-correlated with IR emission. The Vela SNR may be evolving in a a particularly dusty medium, such that the grain evolution is playing a prominent role. It would be interesting to compare the X-ray/IR emission ratio to models constructed for the range of shock velocities and temperatures specific to the Vela SNR.

3.5. Possible Sources of the Enhanced C I* Gas

One possible source of enhanced C I and C I* is mixing of dense cloud material after passage of the shock wave. Poludnenko et al. (2002) have modeled the evolution of multiple dense clouds interacting with a shock wave. The evolution is strongly dependent on the initial separation of the clouds and more weakly dependent on cloud size and density. These models included both a single layer of clouds and multiple layers of clouds from the time of initial contact of the shock with the clouds through cloud expansion, destruction, and ultimate mixing and turbulence. For sufficiently small cloud separations, the clouds will interact during their evolution, possibly merging during the expansion phase. During the last stage, fragmentation caused by Kelvin-Helmholtz instabilities and mixing of the dense cloud material with the shock flow could allow neutral atoms such as C I to enter the shock flow and account for the C I and C I* observed at high-velocity by Jenkins & Wallerstein (1995). The neutral ion cloud material released into the shock flow by fragmentation is expected to accelerate until it co-moves with the shock flow (Klein et al. 1994). Mixing can be quite important because of the relatively short survival time of the dense clouds in the density contrast regime of 10-1000. The combination of high pressure and strong C I implies a scenario of multilayers of small clouds.

Slavin et al. (2004) recently analyzed absorption-line FUSE observations of O VI and IUE observations of C IV toward several of the stars that are reported to show strong C I* in this paper. The observations were compared to steady radiative shock models, and found to be consistent with a shock of velocity 150-200 km s^{-1} propagating into a very inhomogeneous medium. This conclusion supports the concept that the enhanced C I* and associated high pressure are at least in part a result of a clumpy medium in this direction.

If the cloud complex is on the back side of the western hemisphere, as implied by the positive velocities associated with this line of sight (Jenkins & Wallerstein 1995), one consequence of a closely spaced complex of dense clouds might be an "indentation" in this segment of the SNR shell because of the slower expansion velocity of the shock as it passes through the dense clouds. The density contrast will determine the amount of velocity reduction experienced by the shock wave as it passes through the clouds. Clearly, some of the hot gas in the interior of the SNR has expanded without significant interaction with dense clouds, because the western shell is faintly seen in the ROSAT data. The dense clouds could have an impact on the evolution in the western region, as seen in the lower X-ray emission in the region. Only the front hemisphere may have expanded to the west without substantial dense cloud interaction. Also, there may be intercloud regions where the shock blast wave avoids interaction with a dense cloud and continues unimpeded in its expansion around the clouds, if the cloud spacing is large enough.

Thus, one result of a complex of closely spaced clouds would be that the volume of X-ray emitting gas in the line of sight to the western region of the SNR would be reduced and could possibly account for the X-ray discontinuity and reduced emission in this region. Since part of the SNR shell (the near side) would have continued to expand symmetrically from the center of the remnant, unimpeded by dense clouds, the outer shell would be evident, as it is in the ROSAT data. It appears that there are relatively fewer dense clouds in the south of the SNR than in the north.

Another important source of the enhanced C I and C I* could be grain sputtering, as discussed in Section 3.2. Prior to grain destruction by the initial shock wave, grain sputtering will return a significant percentage of C I to the gas. In the case of the Vela SNR, $\sim$ 30% of the carbon is expected to be returned to the gas phase during grain sputtering (Raymond et al. 1997). Because the region we have identified in the western hemisphere has higher column densities of C I and C I* than other regions in the Vela SNR, as least as sampled via absorption lines from background stars, the implication is that this region has either unusually large number of moderately dense clouds, and/or an unusually high dust population.

The velocities of the ground state C I and C I* lines observed toward HD 72089 (Jenkins & Wallerstein 1995) are all positive, indicating the dense clouds and/or dust-enhanced regions are primarily in the back hemisphere of the SNR. The range of velocities observed by Jenkins & Wallerstein (1995) can be explained in several ways. The surface of the shock wave may be "rippled", as in the XA region of the Cygnus Loop. Such an irregular surface would give rise to multiple velocity components along nearby lines of sight. Also, the multiple velocity components detected in C I lines toward HD 72089 may be the result of a thermally unstable shock. Raymond et al. (1991) found that the shock in this region the Vela SNR is thermally unstable; secondary shocks will create multiple velocity components (Innes 1992). Multiple cloud sizes and non-uniform distribution can also generate multiple velocity components in a particular line of sight.

Perhaps a more realistic interpretation of the data is that the C I and /CIstar are produced in a magnetic precursor ahead of the shock front from the supernova. A shock moving into a dense cloud or molecular cloud will have a magnetic precursor if a magnetic field of sufficient strength is present in the cloud (Draine 1980). Such precursors can account for the large amounts of neutral C seen in some lines of sight to the Vela SNR, due to heating of the cloud by the precursor, which can dissociate CO. The presence of a precursor can explain detection of both ions and neutrals in the same line of sight toward a shock, but with different kinematics. Hartigan et al. (2000) found both H_2 and [S II] in a region immediately in front of the shocks in HH168. These authors investigated the HH168 bubble

in Cep A, and found that [S II] leads the Hα at the shock interface, the inverse of what would be expected from shock theory. The [S II] is produced in the precursor, ahead of the shock, in a non-isothermal region. H_2 is present in a zone further from the shock front than the [S II]. Thus, the precursor can be the site of ions, neutrals, and molecules. Depending on the strength of the magnetic field and the shock velocity, the ions can have a different velocity than the neutrals due to ions streaming past the neutrals.

An indication that a magnetic precursor plays an important role in the populations and kinematics of the C I and C I* would be broadened or high-velocity H_2 absorption lines in the directions to the strong C I*. We have FUSE observations of *** of the eleven stars identified with unusually strong /CIstar. The H_2 absorption lines do not appear broadened beyond the instrumental profile in our observations (Slavin et al. 2004). Unfortunately, the FUSE wavelength calibration at the time we did our analysis was not sufficiently reliable to obtain absolute wavelength assignments. The H_2 lines in the FUSE data were actually used to set the relative wavelength scale. We have no information on any velocity offsets of the H_2 lines at this time.

The high dynamic pressure of 2-4 $\times$ 10^{-9} dyne cm^{-2} calculated by Jenkins & Wallerstein (1995) for the line of sight to HD 72089, which lies within the band of strong C I* described in this paper, is greater than the pressure determination toward HD 72088 of 9 $\times$ 10^{-10} dyne cm^{-2} (Raymond et al. 1991). Since the lines of sight to HD 72089 and HD 72088 are separated only by about 3 pc, and both have been identified with strong C I*, the comparison of the pressure values is quite relevant. The factor of 2-4 in the discrepancy between these values, however, may well be explained by the assumptions taken for each calculation. Jenkins & Wallerstein (1995) estimate a shock velocity of 100 km s^{-1}, while Raymond et al. (1991) use a value of 150 km s^{-1}. This alone can be the source of a difference in the pressure of more than a factor of 2, since the pressure scales as the square of the shock velocity. In addition, these calculations use different temperatures and preshock densities in the calculations. If the discrepancy is real, then the pressure is significantly different over path lengths of less than 3 pc. In other regions of the Vela SNR, Raymond et al. (1997) found 1.6 $\times$ 10^{-9} dyne cm^{-2} and Sankrit et al. (2001) found 3.7$\times$ 10^{-10} dyne cm^{-2} near a the location of an X-ray knot in east of the pulsar. At a region near the northern rim of the SNR, Bocchino et al. (2000) found 2.8$\times$ 10^{-10} dyne cm^{-2}. The only other region of the Vela SNR to exhibit characteristics of high pressure of similar magnitude to the band of strong C I* objects is the region near Bullet D, where Sankrit et al. (2003) found a value of 2.6 $\times$ 10^{-9} dyne cm^{-2}.

The concept that the high pressure determined by Jenkins & Wallerstein (1995) could be related to a bullet along the line of sight rather than at a large angle to the line of sight, as is the case with Bullet D, is one possible explanation for the large pressure estimates,

although the large spatial extent of the region of enhanced C I* and thus enhanced pressure suggests multiple bullets would be required to account for the full spatial extent. We believe the high pressure associated with the band of enhanced C I* is more likely a consequence of a complex of moderately dense clouds and/or an very dusty medium local to the narrow line of sight where we found strong C I*.

4. Conclusions

The important finding of this study is that multiple lines of sight in a very limited spatial region toward the Vela SNR exhibit strong interstellar components in the C I* lines. The detection of strong C I* in only a narrow spatial region in the supernova remnant implies a cloud complex interacting with the SNR. The correlation of the C I* with a discontinuity in the X-ray surface brightness in the west suggests the dense clouds responsible for the C I* are engulfed in the supernova remnant and are having an important influence on the evolution. Based on the observations of several positive velocity components in the C I multiplets of HD 72089 reported by Jenkins & Wallerstein (1995) it is plausible that this group of clouds is on the back side of the SNR. Also, the optical and IR morphology of the region where the strong C I* is produced suggests a cloud complex shocked by the blast wave.

Dust temperatures as calculated from a two-component dust model of the entire Vela region based on HIRES IRAS data indicate a portion of the dust emission in this region is inside the supernova remnant. The hot dust shows a correlation with the C I* region as well as optical filaments, and an anti-correlation with X-ray emission. Hot dust temperatures are generally 220-280 K and cold dust temperatures are 15-40° K. The anti-correlation between X-ray and IR emission is an expected result of shock processed dust.

The region of the Vela SNR where we detected strong C I* has been found to be the site of hot dust emission and bright optical emission, as well as being near a discontinuity in the X-ray emission in the western portion of the remnant. A picture emerges of a complex of dense clouds shocked by the supernova blast wave, that are now occupying an internal segment of the SNR sphere on the back side near the western edge. These dense clouds would slow the expansion of the SNR, possibly accounting for the discontinuity in this region of the X-ray surface brightness, although a blowout of the SNR in the western region is another possibility. The dense clouds engulfed by the SNR would create an environment for the production of strong C I* and optical emission, as well as hard X-rays as a result of the reverse shock. Dust sputtering can also produce a significant population of C I as the dust grains are destroyed by the shock wave.

REFERENCES

Aschenbach, B. 1998, Nature, 396, 141

Aumann, H. H., Fowler, J. W., & Melnyk, M. 1990, AJ, 99, 1674

Bocchino, F., Maggio, A., Sciortino, S., & Raymond, J. 2000, A&A, 359, 316

Cha, A. N. & Sembach, K. R. 2000, ApJS, 126, 399

Danks, A. C. & Sembach, K. R. 1995, AJ, 109, 2627

Draine, B. T. 1980, ApJ, 241, 1021

Dubner, G. M., Green, A. J., Goss, W. M., Bock, D. C.-J., & Giacani, E. 1998, AJ, 116, 813

Fesen, R. A., Blair, W. P., & Kirshner, R. P. 1982, ApJ, 262, 171

Fitzgerald, M. P. 1970, A&A, 4, 234

Hartigan, P., Morse, J., & Bally, J. 2000, AJ, 120, 1436

Hobbs, L. M., Ferlet, R., Welty, D. E., & Wallerstein, G. 1991, ApJ, 378, 586

Innes, D. E. 1992, A&A, 256, 660

Jenkins, E. B., Silk, J., Wallerstein, G., & Leep, E. M. 1981, ApJ, 248, 977

Jenkins, E. B., Tripp, T. M., Fitzpatrick, E. L., Lindler, D., Danks, A. C., Beck, T. L., Bowers, C. W., Joseph, C. L., Kaiser, M. E., Kimble, R. A., Kraemer, S. B., Robinson, R. D., Timothy, J. G., Valenti, J. A., & Woodgate, B. E. 1998, ApJ, 492, L147

Jenkins, E. B. & Wallerstein, G. 1995, ApJ, 440, 227

Jenkins, E. B., Wallerstein, G., & Silk, J. 1984, ApJ, 278, 649

Kahn, S. M., Gorenstein, P., Harnden, F. R., & Seward, F. D. 1985, ApJ, 299, 821

Klein, R. I., McKee, C. F., & Colella, P. 1994, ApJ, 420, 213

Lesh, J. R. 1982, in B Stars With and Without Emission Lines, 147–163

Lu, F. J. & Aschenbach, B. 2000, A&A, 362, 1083

McKee, C. F. & Cowie, L. L. 1975, ApJ, 195, 715

Nichols, J. S. & Linsky, J. L. 1996, AJ, 111, 517

Parker, R. A. R., Gull, T. R., & Kirschner, R. P. 1979, An emission-line survey of the Milky Way (NASA SP-434)

Poludnenko, A. Y., Frank, A., & Blackman, E. G. 2002, ApJ, 576, 832

Raymond, J. C., Blair, W. P., Long, K. S., Vancura, O., Edgar, R. J., Morse, J., Hartigan, P., & Sanders, W. T. 1997, ApJ, 482, 881

Raymond, J. C., Wallerstein, G., & Balick, B. 1991, ApJ, 383, 226

Rho, J. & Borkowski, K. J. 2002, ApJ, 575, 201

Saken, J. M., Fesen, R. A., & Shull, J. M. 1992, ApJS, 81, 715

Sankrit, R., Blair, W. P., & Raymond, J. C. 2003, ApJ, 589, 242

Sankrit, R., Shelton, R. L., Blair, W. P., Sembach, K. R., & Jenkins, E. B. 2001, ApJ, 549, 416

Seward, F. D. 1988, BAAS, 20, 1049

Slavin, J. D., Nichols, J. S., & Blair, W. 2004, ApJ, accepted

Smith, M. A. 2001, PASP, 113, 882

Vancura, O., Raymond, J. C., Dwek, E., Blair, W. P., Long, K. S., & Foster, S. 1994, ApJ, 431, 188

Walborn, N. R., Heckathorn, J. N., & Hesser, J. E. 1984, ApJ, 276, 524

Walborn, N. R. & Hesser, J. E. 1982, ApJ, 252, 156

Wallerstein, G., Jenkins, E. B., & Silk, J. 1980, ApJ, 240, 834

Wallerstein, G. & Silk, J. 1971, ApJ, 170, 289

Wallerstein, G., Vanture, A., & Jenkins, E. B. 1995, ApJ, 455, 590

White, R. L. & Long, K. S. 1991, ApJ, 373, 543

This preprint was prepared with the AAS LaTeX macros v5.0.

Table 1. Stars Observed in the Vela SNR Region

Star	ra J2000	dec J2000	Spec. Type	distance Spect.	distance Hipparcos	SWP	Obs. Date
HD 68243	08 09 29.33	-47 20 43.0	B1 IV	400	$\cdots$	32408	11/27/99
HD 68273	08 09 31.95	-47 20 11.7	WC	$\cdots$	$258_{+41,-31}$	43022	11/06/91
HD 69404	08 14 51.24	-46 29 09.2	B3 Vnne	376	$408_{+127,-78}$	05534	06/15/79
HD 69648	08 16 02.74	-44 19 21.7	O8.5 Iab:	3602	$\cdots$	25707	04/17/85
HD 69973	08 17 19.58	-47 55 12.3	B5 Vn	335	$417_{+132,-81}$	05511	06/13/79
HD 70084	08 18 01.15	-47 05 30.7	B7 III	501	$389_{+129,-77}$	20860	08/31/83
HD 70309	08 19 05.58	-48 11 52.3	B3 V	374	$253_{+40,-31}$	05530	06/15/79
HD 70930	08 22 31.69	-48 29 25.4	B1 V	348	$463_{+166,-97}$	05531	06/15/79
HD 71019	08 23 25.23	-42 48 26.2	B3 II/III	$\cdots$	$\cdots$	09434	07/03/80
HD 71216	08 24 35.28	-40 44 49.2	B5 Vn	448	$441_{+140,-86}$	20191	06/11/83
HD 71336	08 25 06.98	-43 21 52.7	B3 V	724	$\cdots$	09433	07/03/80
HD 71459	08 25 51.91	-42 09 11.1	B3 V	242	$249_{+36,-27}$	05533	06/15/79
HD 72014	08 28 52.06	-42 35 14.9	B3 Vnne	400	$926_{+860,-301}$	05495	06/11/79
HD 72067	08 29 07.57	-44 09 37.5	B2 V	$\cdots$	$490_{+219,-115}$	29376	10/05/86
HD 72088	08 29 12.64	-44 53 05.6	B3 III/IV	1630	$\cdots$	38714	05/01/91
HD 72089	08 29 06.97	-45 33 26.9	B5 II/III	$\cdots$	$\cdots$	14096	05/28/81
HD 72127A	08 29 27.00	-44 43 30.0	B2 IV	230	$\cdots$	43030	11/08/91
HD 72179	08 29 37.73	-44 05 58.0	B4 II/III	1574	$\cdots$	14117	05/30/81
HD 72230	08 29 51.24	-44 44 36.0	B9 V	$\cdots$	$\cdots$	14118	05/30/81
HD 72350	08 30 39.23	-44 44 14.4	B4 V	281	$685_{+581,-216}$	44774	05/25/92
HD 72537	08 31 36.69	-45 47 05.2	B3 V	$\cdots$	$377_{+104,-66}$	05529	06/15/79
HD 72555	08 31 39.65	-47 14 27.7	B2.5 V	590	$394_{+111,-71}$	05555	06/17/79
HD 72648	08 32 18.99	-43 55 53.4	B1/B2 Ib	3178	$741_{+708,-243}$	14126	05/30/81
HD 72754	08 32 23.38	-49 36 04.8	B2 Ia:pshe	$\cdots$	$690_{+545,-182}$	05888	09/22/79
HD 72798	08 33 01.86	-45 45 10.	B3 III	$\cdots$	$752_{+530,-220}$	14102	05/28/81
HD 72997	08 34 08.14	-44 32 41.4	B2 II/III	2173	$621_{+454,-184}$	05549	06/17/79
HD 73010	08 34 11.12	-45 38 11.7	B5 V	$\cdots$	$746_{+683,-241}$	05550	06/17/79
HD 73882	08 39 09.53	-40 25 09.3	O8 V:	968	$500_{+719,-186}$	38311	03/06/90
HD 74194	08 40 47.79	-45 03 30.2	O9	2213	(2777)	05527	06/15/79
HD 74234	08 40 53.40	-48 13 31.8	B2 V	677	$629_{+351,-166}$	05491	06/11/79
HD 74273	08 41 05.32	-48 55 21.6	B1.5 V	519	$4230_{+219,-115}$	05494	06/11/79
HD 74319	08 41 34.90	-44 59 30.9	B3 V	394	$402_{+113,-73}$	05505	06/13/79
HD 74436	08 42 07.55	-48 14 40.8	B3 V	786	$412_{+523,-148}$	05525	06/15/79
HD 74530	08 42 36.55	-48 04 30.9	B3 IV/V	1226	$\cdots$	05487	06/11/79
HD 74580	08 42 53.07	-48 07 41.2	B3 V	872	$\cdots$	05488	06/11/79
HD 74620	08 43 07.03	-47 41 12.9	B4	907	$\cdots$	05504	06/13/79
HD 74662	08 43 18.80	-48 20 42.9	B3 V	1008	$\cdots$	05526	06/15/79

Table 1—Continued

Star	ra J2000	dec J2000	Spec. Type	distance Spect.	distance Hipparcos	SWP	Obs. Date
HD 74711	08 43 47.51	-46 47 56.4	B2 III	1004	$\cdots$	14125	05/30/81
HD 74753	08 43 40.27	-49 49 22.1	B0 IIIn	977	$465_{+168, -97}$	05557	06/17/79
HD 74773	08 44 09.71	-47 06 58.0	B3 IV	735	$840_{+799,-275}$	05553	06/17/79
HD 74920	08 45 10.34	-46 02 19.2	O8	3130	$\cdots$	05559	06/17/79
HD 75129	08 46 19.41	-47 32 59.6	B5 Ib	1725	$503_{+182,-106}$	14123	05/30/81
HD 75149	08 46 30.55	-45 54 45.0	B3 Ia	1780	$1010_{+12127-356}$	07726	01/21/80
HD 75309	08 47 27.97	-46 27 04.0	B2 Ib/II	3170	$\cdots$	14124	05/30/81
HD 75549	08 49 03.36	-43 45 40.4	B3 V	556	$330_{+87,-57}$	14104	05/28/81
HD 75759	08 50 21.02	-42 05 23.2	O9 V	929	$585_{,+262, -139}$	06397	09/05/79
HD 75821	08 50 33.46	-46 31 45.1	B0 III	964	$826_{+623,-248}$	05560	06/17/79
HD 76161	08 52 38.61	-48 21 32.8	B3 Vn	296	$333_{+70,-49}$	06635	09/26/79
HD 76341	08 54 00.61	-42 29 08.8	O9 III	1471	$1220_{+3780,-526}$	28157	04/12/86
HD 76534	08 55 08.71	-43 27 59.9	B3 Vne	271	$412_{+473,-144}$	47830	06/08/93
HD 76536	08 54 59.17	-47 35 32.7	WC		(3448)	10113	09/13/80
HD 76566	08 55 19.20	-45 02 30.0	B3 IV	189	$287_{+60,-43}$	14121	05/30/81
HD 78616	09 07 42.52	-44 37 56.8	B2 II/III	1265	(1250)	10804	12/12/80

Table 2.   Velocity Displacement of C I Multiplets

Wavelength (Å)	State	Velocity Displacement from Neutral (km s^{-1})
1277.2454	$^3P_0$	0.0
1277.2823	$^3P_1$	8.7
1277.5130	$^3P_1$	62.9
1277.5496	$^3P_2$	71.5
1277.7229	$^3P_2$	112.2
1277.9538	$^3P_2$	166.4
1328.8333	$^3P_0$	0.0
1329.0853	$^3P_1$	56.9
1329.1004	$^3P_1$	60.3
1329.1233	$^3P_1$	65.5
1329.5775	$^3P_2$	168.0
1329.6005	$^3P_2$	173.2
1560.3092	$^3P_0$	0.0
1560.6822	$^3P_0$	71.7
1560.7090	$^3P_1$	76.9
1561.3402	$^3P_2$	198.2
1561.3667	$^3P_2$	203.3
1561.4384	$^3P_2$	217.1
1656.2672	$^3P_1$	−119.7
1656.9283	$^3P_0$	0.0
1657.0082	$^3P_1$	14.5
1657.3793	$^3P_1$	81.6
1657.9068	$^3P_1$	177.2
1658.1212	$^3P_2$	216.0

Table 3.   Stars Showing Strong High Excitation C I

Star	Distance pc		Observed Line Velocity (km s^{-1})			
	Hip.	Sp.	1277Å	1329Å	1561Å	1657Å
HD 70309	253$_{+40,-31}$	374	$\cdots$	$\cdots$	$\cdots$	+26
			+94	+105	$\cdots$	$\cdots$
HD 71459	249$_{+36,-27}$	242	+13	+17	+16	+26
			+97	+84	+105	+108
HD 71336	$\cdots$	724	+32	+25	+29	+36
			+122	+100	+118	+126
HD 72014	926$_{+860,-301}$	400	+20	+30	$\cdots$	+33
			$\cdots$	$\cdots$	+116	$\cdots$
HD 72127A	$\cdots$	230	+10	$\cdots$	+9	+21
			+64	+71	+89	$\cdots$
HD 72088	$\cdots$	1630	+30	+30	+20	+30
			$\cdots$	+81	+95	$\cdots$
HD 72350	685$_{+581,-216}$	281	+39	+36	+40	+46
			$\cdots$	+96	+115	+124
HD 72537	377$_{+104,-66}$	$\cdots$	+18	+22	+34	+21
			+93	$\cdots$	+92	$\cdots$
HD 72648	741$_{+708,-243}$	3178	+36	+28	+37	+39
			$\cdots$	+90	+103	$\cdots$
HD 72555	394$_{+111,-71}$	590	+32	+24	+11	+23
			$\cdots$	$\cdots$	+99	$\cdots$
HD 74662	$\cdots$	1010	+30	+26	+24	$\cdots$
			+94	$\cdots$	$\cdots$	$\cdots$

Table 4. Radial Velocity of C I

Star	Velocity km s^{-1}
HD 72179	+12
HD 72648	+27
HD 72350	+12
HD 72088	+12,+26
HD 72997	+35
HD 72089	+24
HD 72798	+22
HD 72319	+62
HD 74194	+12
HD 72555	+22
HD 75149	+18
HD 74920	+11
HD 76566	+23
HD 74530	+17
HD 74580	+14
HD 78616	+18
HD 72754	+12
HD 76161	+8
HD 74753	+45
HD 74195	+16

Table 5.   Dust temperatures for regions in IRAS temperature map

Region	# good pixels (hot)	T_{hot} K	# good pixels (cold)	T_{cold} K
1	51	70	310	27
2	87	220	193	17
3	1244	223	1244	25
4	310	242	310	23
5	0	0	310	38
6	271	265	298	16